NOVEL METHODS AND ANALYSIS OF B_0 AND B_1 GRADIENTS IN MAGNETIC RESONANCE IMAGING

A DISSERTATION SUBMITTED TO
THE DEPARTMENT OF ELECTRICAL AND ELECTRONICS ENGINEERING
AND THE GRADUATE SCHOOL OF ENGINEERING AND SCIENCE
OF BILKENT UNIVERSITY
IN PARTIAL FULFILLMENT OF THE REQUIREMENTS
FOR THE DEGREE OF
DOCTOR OF PHILOSOPHY

By
Esra Abacı Türk
June, 2013

I certify that I have read this thesis and that in my opinion it is fully adequate, in scope and in quality, as a dissertation for the degree of Doctor of Philosophy.

Prof. Dr. Ergin Atalar (Advisor)

I certify that I have read this thesis and that in my opinion it is fully adequate, in scope and in quality, as a dissertation for the degree of Doctor of Philosophy.

Prof. Dr. Yusuf Ziya İder (Co-Advisor)

I certify that I have read this thesis and that in my opinion it is fully adequate, in scope and in quality, as a dissertation for the degree of Doctor of Philosophy.

Prof. Dr. Hayrettin Köymen

I certify that I have read this thesis and that in my opinion it is fully adequate, in scope and in quality, as a dissertation for the degree of Doctor of Philosophy.

Prof. Dr. Ömer Morgül

I certify that I have read this thesis and that in my opinion it is fully adequate, in scope and in quality, as a dissertation for the degree of Doctor of Philosophy.

Assoc. Prof. Dr. A. Sanlı Ergün

I certify that I have read this thesis and that in my opinion it is fully adequate, in scope and in quality, as a dissertation for the degree of Doctor of Philosophy.

Assoc. Prof. Dr. Yeşim Serinağaoğlu Doğrusöz

Approved for the Graduate School of Engineering and Science:

Prof. Dr. Levent Onural
Director of the Graduate School

ABSTRACT

NOVEL METHODS AND ANALYSIS OF B_0 AND B_1 GRADIENTS IN MAGNETIC RESONANCE IMAGING

Esra Abacı Türk
Ph.D. in Electrical and Electronics Engineering
Supervisors: Prof. Dr. Ergin Atalar and Prof. Dr. Yusuf Ziya İder
June, 2013

In this thesis, analysis of B_0 gradients and B_1 fields are performed and novel methods using B_1 gradients instead of B_0 gradients are proposed. The first contribution of this dissertation is expressing the nature of the interaction between the B_0 gradient fields and the active implantable medical devices (AIMD). By utilizing the fact that gradient coils produce linear magnetic field in a volume of interest, the simplified closed form electric field expressions are defined inside a homogeneous cylindrical volume. Using these simplified expressions, the induced potential on an implant electrode has been computed approximately for various lead positions on a cylindrical phantom and verified by comparing with the measured potentials for these sample conditions. In addition, the validity of the method has been tested with isolated frog leg stimulation experiments. The results of both phantom and ex vivo experiments show that if the path of the implant lead is known, the induced voltage on the lead can be estimated analytically. The second topic in this dissertation is the Bloch-Siegert (BS) shift based B_1 mapping method. The method is analyzed in terms of the effects of the off-resonance frequency, the RF pulse shape, and the duration of the RF pulse. Based on these analyses, a new theoretical model that relates the Fourier transform of the off-resonant BS RF pulse envelope to the phase shift is proposed. Utilizing Bloch simulations and phantom experiments the proposed frequency domain expression is verified. The results indicates that the proposed expression works well even for short pulse durations ($< 2ms$) and low offset frequencies ($f_{RF} < 500Hz$) when the ratio of the RF field and the frequency offset of the RF pulse is smaller than 0.5. The last topic of this dissertation is on flow and shear wave imaging with B_1 gradients instead of B_0 gradients. In flow imaging, a novel sequence using a Bloch-Siegert pulse generated by a spatially dependent B_1 field is proposed. The proposed method is experimentally verified by comparing the resultant velocity measurements with those obtained by using bipolar flow

encoding B_0 gradients. This comparison demonstrates the feasibility of using BS shift with B_1 gradients in detecting the flow. The usage of B_1 gradients is also proposed to detect shear waves at frequencies in kilohertz range and this method is experimentaly verified for 2kHz, 3kHz and 4kHz shear frequencies. The studies in this thesis indicate that extensive analysis of B_0 gradients in Magnetic Resonance Imaging (MRI) is important for safety issues, and for scenarios where B_0 gradients prove insufficient in encoding due to hardware limitations, utilizing B_1 gradients can be considered as an alternative.

Keywords: MRI, B_0 gradients, B_1 gradients, shear wave imaging, flow imaging.

ÖZET

MR GÖRÜNTÜLEMEDE KULLANILAN B_0 VE B_1 GRADYANLARIN İNCELENMESİ VE YENİ YÖNTEMLER

Esra Abacı Türk
Elektrik Elektronik Mühendisliği, Doktora
Tez Yöneticileri: Prof. Dr. Ergin Atalar ve Prof. Dr. Yusuf Ziya İder
Haziran, 2013

Bu tezde, B_0 gradyanlar ve B_1 alanlar incelenmiş, B_1 gradyanların, B_0 gradyanlar yerine kullanıldığı yeni yöntemler sunulmuştur. Bu tezin katkılarından ilki, gradyan alanlar ile aktif medikal implantlar arasındaki ilişkinin incelenmesiyle ilgilidir. Görüntülenecek bölgede gradyan sargıların yarattığı manyetik alanın doğrusal olması bilgisinden yararlanılarak, homojen silindirik bir hacim içerisinde basitleştirilmiş elektrik alan denklemleri elde edilmiştir. Bu denklemler kullanılarak, silindirik bir fantom içerisinde farklı implant kablosu pozisyonlarında elektrod üzerinde indüklenebilecek potansiyel yaklaşık olarak hesaplanmış ve deneysel ölçümlerle karşılaştırılarak doğrulanmıştır. Bunun yanında, izole edilmiş kurbağa bacağı deneyleri ile de metodun doğruluğu test edilmiştir. Deney sonuçları, implant kablosunun pozisyonu bilindiğinde, kablo üzerinde indüklenebilecek voltajın yaklaşık olarak hesaplanabileceğini göstermiştir. Tezin ikinci konusu Bloch-Siegert (BS) faz kaymasndan yararlanan B_1 haritalama tekniğidir. Kullanılan frekansın rezonans frekansından kayma miktarının, kullanılan RF pulsun şeklinin ve süresinin yönteme etkisi incelenmiştir. Bu analizler sonucunda BS RF pulsun Fourier transformu ile elde edilen faz kayması arasında yeni bir teorik model sunulmuştur. Bloch simülasyonları ve fantom deneyleri ile önerilen yöntemin doğruluğu test edilmiştir. RF alanı ile frekans kayması arasındaki oran 0.5'ten küçük olduğunda, sonuçlar önerilen denklemin kısa BS RF puls uzunluklarında ($< 2ms$) ve düşük frekans kaymalarında ($f_{RF} < 500Hz$) dahi doğru çalıştığını göstermiştir. Tezin son konusu B_1 gradyanlar kullanılarak akış ve kesme dalga haraketinin görüntülenmesi ile ilgilidir. Akış hareketinin gözlenmesinde, uzaysal değişkeni olan B_1 alanlarla oluşturulan BS pulsunun kullanıldığı yeni bir sekans önerilmiştir. Önerilen yöntemin deneysel sonuçları günümüzde kullanılmakta olan yöntem sonuçları ile karşılaştırılarak

doğrulanmıştır. Bu karşılaştırma B_1 gradyanların, akış görüntülemede kullanılabilirliğini göstermiştir. Aynı zamanda, B_1 gradyanların kilohertz seviyesindeki frekanslarda kesme dalga hareketinin görüntülenmesinde kullanılması önerilmiştir. Bu yöntem, 2kHz, 3kHz ve 4kHz kesme dalga frekansları için denenmiştir. Tezdeki çalışmalarda, MR güvenliği için B_0 gradyanlar incelenmiş ve çeşitli kısıtlamalar sebebiyle B_0 gradyanların kullanılamadığı durumlarda B_1 gradyanların kullanılabileceği gösterilmiştir.

Anahtar sözcükler: MRI, B_0 gradyanlar, B_1 gradyanlar, kesme dalga görüntüleme, akış görüntüleme.

Acknowledgement

It is my great pleasure to thank all the colleagues, collaborators and friends who made this thesis possible. First, I would like to thank to Ergin Atalar. He has not only guided my research work, but also has been a supportive mentor and like a second father. When I have been too close to give up on my PhD, our conversations have motivated me. I owe my deepest gratitude to him.

I would like to thank Y. Ziya İder and Sanlı Ergün for their valuable discussions throughout my PhD studies. Having a chance to work with them is a great honour for me. I also want to thank my jury members; Hayrettin Köymen and Ömer Morgül for all their comments on my work, and Yeşim Serinağaoğlu for reading and commenting on this dissertation.

I want to acknowledge The Scientic and Technological Research Council of Turkey (TÜBİTAK) for supporting the work done in this thesis.

I would like to thank to my colleagues Yiğitcan Eryaman, Emre Kopanoğlu, Volkan Açıkel, Ali Çağlar Özen, Cemre Arıyürek and Taner Demir who make our research center, UMRAM not only a place to work but also a place to live. I would like to thank Uğur Yılmaz, Yıldıray Gökhalk and Umut Gündoğdu for all the scientific collaborations. I would like to thank Aydan Erçingöz for all the small talks, and Mürüvet Parlakay for all her help throughout my years at Bilkent. I also want to thank my old and new friends from UMRAM, Bilkent University and Middle East Technical University as well.

I would like to thank my big-hearted family for all their love and encouragement. Without their love and condence to me, I could not manage to finish this study.

Last but not least, I would like to thank to my dear husband Ata Türk who has shared all the burden with me. He has become a rock in my life sometimes to rest, sometimes to hide.

Contents

List of Figures

Chapter 1

Introduction

Magnetic resonance imaging (MRI) is one of the most widely used imaging technique for clinical purposes due to its high soft tissue contrast. Besides, it is a non-ionizing radiation technique which makes it more preferable than the other imaging techniques. However, still extensive analyses and improvements need to be done to make this imaging tool safer and to enhance its application areas.

In this study, we first provide a derivation of simplified expressions for the electric field inside the cylindrical homogeneous body model for a perfectly uniform gradient field [1]. These expressions can be used to understand the nerve stimulation risk for patients with active implantable medical devices (AIMD). During MRI, the rapidly switched gradient magnetic field induces an electric field and the magnitude of this field is proportional with the rate of change of the magnetic field. Since the human nervous system is sensitive to the field variations at low frequencies [2], an induced electric field may cause nerve stimulation. Previously, the peripheral nerve stimulation risk has been investigated theoretically and experimentaly in the absence of any metallic implant [3–10]. The studies [11–14] show that a time-varying magnetic field causes stimulation by inducing an electric field on an AIMD inside the human body. However, there is no method in the literature that provides intuitive information about the stimulation risk when there is an AIMD. Hence, in this study, a closed-form expressions of electric and magnetic fields for a linear gradient field formed by an infinitely long cylindrical

gradient coil is proposed and used to estimate an induced potential along an implant lead by assuming a unipolar pacing model. The accuracy of the proposed expressions in estimating the stimulation risk is tested with ex vivo frog nerve experiments.

Our second contribution is on analysis of Bloch-Siegert shift B_1 mapping method [15]. We also present a new approximated Fourier domain expression to increase the understandability of the method [16]. B_1 mapping is generally used (i) to adjust a specific flip-angle for RF pulses, (ii) to design multichannel RF pulses, (iii) to obtain T_1 maps, (iv) to obtain conductivity maps, and (v) to calculate local specific absorption rate (SAR). The Bloch-Siegert (BS) shift based B_1 mapping technique is a phase based technique [17]. This technique has a fast acquisition time. Furthermore, it is insensitive to spin relaxation, repetition time (TR), starting flip angle, chemical shift, and B_0 field inhomogeneities. Due to these properties, BS shift based B_1 mapping became a widely used technique in a very short time. On the other hand, relatively long off-resonant RF pulse used to create the BS phase shift may cause high SAR and signal loss due to the $T2^*$ and $T2$ effects. The usage of a short pulse duration for BS pulses becomes important to minimize these problems. In this study, we first investigated the relationship between the effects of the off-resonance frequency, the RF pulse shape, and the duration of the RF pulse. To this end, a general expression based on theoretical modeling that relates the Fourier transform of the off-resonant BS RF pulse envelope to the phase shift is proposed. To verify the accuracy of the proposed expression, extensive Bloch simulations and phantom experiments are performed.

Our final contribution is on imaging of flow and shear waves using B_1 gradients instead of B_0 gradients. MR imaging is not only used to provide structural information, but also information about blood flow, and tumor kinetics can be obtained with MR imaging. Currently, the blood flow imaging is performed by using bipolar flow encoding gradients to characterize the cardiovascular functions [18–21]. In this study, a novel solution to encode flow is proposed. In this method, Bloch-Siegert (BS) phase shifts generated by a spatially dependent B_1 field is used to encode flow. The results of the experiments demonstrate that flow detection by using BS shift with B_1 gradients is feasible. Similarly, magnetic

resonance elastography (MRE) is a non-invasive phase contrast based imaging technique used for the visualization of elastic properties of biological tissues [22]. Wave images can be obtained from MR phase images when motion sensitization gradients (MEGs) are synchronized with the shear wave excitation pulse generated by an electromechanical actuator [23]. Due to the gradient amplitude and slew rate limitations of the MR system, in order to detect the stiffness of a very small and stiff tissues (e.g. hyaline cartilage tissue), a new gradient coil has to be constructed [24]. But using gradient coils at higher frequencies causes an increase in the eddy currents induced by fast switching rates, and also it causes an increase in the noise induced by the gradient coils. In this study, to use RF fields with high B_1 gradients and a phase, alternating between 0 and π is proposed to encode wave motion. With this alternative method, the limitations due to finite rise- and fall-time of the gradient waveforms and therefore the maximum frequency of the wave that can be detected in the tissue can be solved. The observed signal with this method is only due to the motion and therefore the displacement of the shear wave can be calculated by using the magnitude image. To verify the method, MR experiments are performed by using agar phantoms at frequencies in the kilohertz range.

The structure of the dissertation is as follows. In the second chapter, the derivations of a simple analytical expression for the gradient induced potential and the experimental verification are discussed. The third chapter is about the analysis of the Bloch-Siegert shift B_1 mapping method and in the same chapter, the derivations of a new approximated Fourier domain expression are presented. The fourth chapter presents novel methods using B_1 gradient for flow and shear wave imaging. Finally, we conclude in the fifth chapter.

Chapter 2

A Simple Analytical Expression for the Gradient Induced Potential on Active Implants During MRI

2.1 Preface

The content of this chapter was presented in part at the Scientic Meetings of International Society of Magnetic Resonance in Medicine [25] and it was published in IEEE Transaction on Biomedical Engineering [1]. The text and the figures of this chapter are based on the journal publication.

2.2 Introduction

Although magnetic resonance imaging (MRI) is known to be a very safe diagnostic technique, patients with active implantable medical devices (AIMD) are generally not allowed to be scanned because of the undesirable interaction between the

electromagnetic field generated by the MRI scanner and AIMD. While the effects of static magnetic and radio-frequency electromagnetic fields have been widely studied, the interaction between the implants and the gradient magnetic field has not been studied in depth.

In MRI, gradient waveforms are usually designed as pulses. Their ramp up and down times are usually considered as dead times and minimized for maximum performance. On the other hand, a rapidly switched gradient magnetic field induces an electric field inside the body that may cause nerve stimulation [26]. In the presence of an AIMD, the risk of stimulation increases [12]. In particular, when a cardiac pacemaker or an implantable cardioverter-defibrilator is present in the patient during an MRI examination, possibility of cardiac arrest is a very serious concern [13, 14].

To investigate the peripheral nerve stimulation risk and the threshold value, in the absence of any metallic implant, theoretical and experimental studies have been carried out [3–10]. In these studies, electric field distributions are analyzed for theoretical explanations of the stimulation risk. For the electric field measurements, field probe is used in [10]. However it is useful only for the measurement of the induced electric field at the body boundary. Furthermore, to define the induced electric field, both computational methods such as finite difference time domain [6], and analytical calculations have been performed using inhomogeneous and homogeneous human models [3, 27, 28]. The studies [11–14] show that a time-varying magnetic field causes stimulation by inducing an electric field on an AIMD inside the human body. However, in [11, 12], no experimental verification is performed and in [13], experiments are only performed for Helmholtz coil. On the other hand, in [14], experiments were performed on six mongrel dogs and the induced current was measured with a current recorder. However, no analytical explanation about the stimulation risk is carried out.

In a safety analysis of AIMD during an MRI examination, a generic and simple formulation of the induced potential on electrodes of AIMD has a critical importance. This will give an insight on the worst case conditions for implants. With

this simple formulation of the induced potential on electrodes and the knowledge of the lead impedance, the appropriate filter for leads to protect the patient from the stimulation risk during MRI may also be designed. Although in [27] the induced electric and magnetic field expressions were derived for a homogeneous cylindrical body model so that the induced potential on an electrode can be found, the provided expressions involve complicated Fourier integrals to be calculated numerically. Hence, they are not suitable for obtaining a generic and simple induced potential expression.

Therefore, in this study, we provide closed-form expressions of electric and magnetic fields for a linear gradient field formed by an infinitely long cylindrical gradient coil. With the simplified field expressions, induced potential causing stimulation is estimated by assuming a unipolar pacing model. We conducted phantom experiments to compare the difference between our estimated and actually measured potential values, and we also tested the accuracy of our expressions in estimating the stimulation risk with ex vivo frog nerve experiments. Experimental results show that, using the simplified expressions, we can determine the voltage induced on the implant lead if the path of the implant lead is known.

2.3 Theory

To estimate the stimulation risk, we need to calculate the induced voltage on the implant lead, which can be deduced from the induced electric field distribution. During the ramping up and ramping down periods of the gradient fields an induced electric field $\vec{E}$, is set up in the medium. If there is an implant lead in the medium, insulated except for the tips and extended in the direction of $\vec{E}$, then charge accumulates at the tips immediately to generate an opposing electric field. The total electric field is equal to the sum of the magnetically induced electric field and the charge induced electric field. Near the tip of the lead the charge induced electric field is the dominating one and furthermore because it has steep variation near the tip it is the cause of stimulation of a nearby nerve membrane [29].

The amount of current leaving the lead and flowing in the medium due to the charge induced electric field is determined by the charge induced potential difference between the two ends of the implant lead divided by the impedance which is the sum of the contact impedance and the equivalent impedance of the medium. This voltage difference can be calculated by integrating the charge induced electric field along the path of the lead. This integral on the other hand is equal to the negative of the integral of the magnetically induced electric field along the path of the lead, since inside the lead the total electric field is almost zero. This stimulation can be likened to the working of a unipolar pacing system, where there is a lead connecting the only electrode within the heart with a metal casing supplying power.

In [27], to calculate the electric field $\vec{E}$, first the scalar potential V, and the vector potential $\vec{A}$ inside the gradient coil have been solved by applying an appropriate boundary condition on the surface of a cylindrical volume. It is assumed that the conductivity of the volume is uniform and nearly equal to the average of the conductivity of tissues inside the body as done in similar studies on the subject. Moreover, since the gradient magnetic field is a low frequency field, skin depth is assumed to be much larger than the physical size of the stimulated tissue region, which means that the induced current inside the body is not a source to generate magnetic field. Similarly, for low-frequencies, the displacement current is also ignored. Under these assumptions the scalar and the vector potential equations have been simplified and utilized to provide the electric and the magnetic field expressions inside the body in [27]. However, the field expressions provided in [27] are defined in terms of their Fourier transforms and the coil current distribution is required for the computational analysis of the field distributions.

In this study, we provide generic simplified electric and magnetic field expressions that do not require the current distribution to be known in advance. In addition to the same assumptions with [27], we also assumed that the gradient coil is infinitely long, in other words, gradient field is linear in everywhere.

According to the general principle of the target field method, for a specified target field on a cylindrical surface with radius c (i.e., $\rho = c$), the Fourier transform of the current flowing in ϕ-direction can be found as the following [30]:

$$J_{\phi}^{(m)}(k) = -\frac{B_z^{(m)}(c,k)}{\mu_0 k a I_m(kc) K'_m(ka)} \qquad c \leq a \tag{2.1}$$

where $B_z^{(m)}(c,k)$ is the Fourier transform of the target magnetic field in z-direction over a cylindrical surface with radius c; $I_m(kc)$ and $K_m(ka)$ are the first and the second kind modified Bessel functions of order m; k is spatial frequency; a is the radius of the coil; and μ_0 is the permeability of the medium.

As the design parameter, the z-component of the magnetic field is given as $B_z = xG_x + yG_y + zG_z$, where G_x, G_y and G_z are the gradient fields in the x-,y- and z-directions, respectively. For imaging purposes, G_x, G_y and G_z are constant within the volume of interest. In order to define the target magnetic fields in the z-direction for x-, y-, and z-gradient coils, the $g(z)$ function that describes the field variation in the z-direction can be added to the predefined B_z field expression [31]. Simplification of the field expressions is performed by using these target fields.

For x-gradient coil, the target field is taken as $B_z(c,\phi,z) = xG_x g(z) = c\cos\phi G_x g(z)$. To find $J_{\phi}^{(m)}(k)$, first the Fourier transform, $B_z^{(m)}(c,k)$ for the given target field is defined as follows:

$$\begin{aligned} B_z^{(m)}(c,k) &= \frac{1}{2\pi}\int_{-\infty}^{\infty}\int_{-\pi}^{\pi} e^{-im\phi}e^{-ikz}B_z(c,\phi,z)d\phi dz \\ &= \frac{1}{2\pi}\int_{-\infty}^{\infty}\int_{-\pi}^{\pi} e^{-im\phi}e^{-ikz}G_x g(z) c\cos\phi d\phi dz \\ &= G_x c\frac{\delta_{-1m}+\delta_{1m}}{2}\int_{-\infty}^{\infty} g(z)e^{-ikz}dz \\ &= G_x c\frac{\delta_{-1m}+\delta_{1m}}{2}\bar{g}(k), \end{aligned} \tag{2.2}$$

where $\bar{g}(k) = \int_{-\infty}^{\infty} g(z)e^{-ikz}dz$, the Kronecker symbol δ_{jm} has the value 1 if $j = m$ and 0 otherwise, and $i = \sqrt{-1}$. By inserting this $B_z^{(m)}(c,k)$ field into (2.1), the expression for $J_{\phi}^{(m)}(k)$ is as follows:

$$J_{\phi}^{(m)}(k) = -\frac{G_x c(\delta_{-1m}+\delta_{1m})\bar{g}(k)}{2\mu_0 k a I_m(kc) K'_m(ka)}. \tag{2.3}$$

Eq. (2.3) is used in the field expressions defined for a cylindrical volume with radius ρ_0 given in [27], and the field components in the form of Fourier transforms are derived. Before starting the simplification, the inverse Fourier transform of each component is expressed as follows:

$$\begin{aligned}
E_\rho(\rho,\phi,z) &= -\omega G_x \frac{1}{2\pi}\sum_{m=-\infty}^{\infty} e^{im\phi}\int_{-\infty}^{\infty} e^{ikz}(\delta_{-1m}+\delta_{1m})\frac{m\bar{g}(k)}{2k^2}\frac{c}{I_m(kc)} \\
&\quad \times\Big(\frac{I_m(k\rho)}{\rho} - \frac{I_m(k\rho_0)I'_m(k\rho)}{\rho_0 I'_m(k\rho_0)}\Big)dk, \qquad (2.4)\\
E_\phi(\rho,\phi,z) &= -i\omega G_x \frac{1}{2\pi}\sum_{m=-\infty}^{\infty} e^{im\phi}\int_{-\infty}^{\infty} e^{ikz}(\delta_{-1m}+\delta_{1m})\frac{\bar{g}(k)}{2k}\frac{c}{I_m(kc)} \\
&\quad \times\Big(I'_m(k\rho) - \frac{m^2 I_m(k\rho_0)I_m(k\rho)}{k^2\rho\rho_0 I'_m(k\rho_0)}\Big)dk, \qquad (2.5)\\
E_z(\rho,\phi,z) &= -i\omega G_x \frac{1}{2\pi}\sum_{m=-\infty}^{\infty} e^{im\phi}\int_{-\infty}^{\infty} e^{ikz}(\delta_{-1m}+\delta_{1m})\frac{mI_m(k\rho_0)}{2k^2\rho_0 I'_m(k\rho_0)} \\
&\quad \times\frac{cI_m(k\rho)}{I_m(kc)}\bar{g}(k)dk, \qquad (2.6)\\
B_\rho(\rho,\phi,z) &= -iG_x \frac{1}{2\pi}\sum_{m=-\infty}^{\infty} e^{im\phi}\int_{-\infty}^{\infty} e^{ikz}(\delta_{-1m}+\delta_{1m})\frac{cI'_m(k\rho)}{2I_m(kc)} \\
&\quad \times\bar{g}(k)dk, \qquad (2.7)\\
B_\phi(\rho,\phi,z) &= G_x \frac{1}{2\pi}\sum_{m=-\infty}^{\infty} e^{im\phi}\int_{-\infty}^{\infty} e^{ikz}(\delta_{-1m}+\delta_{1m})\frac{mc}{2k\rho} \\
&\quad \times\frac{I_m(k\rho)}{I_m(kc)}\bar{g}(k)dk. \qquad (2.8)
\end{aligned}$$

Note that, the expressions will be different than 0, only for $m = 1$ and $m = -1$ indices due to the Kronecker delta functions δ_{-1m} and δ_{1m}.

The function $g(z)$, describing the z variation of the magnetic field, has to be chosen as given in [30] to satisfy the current continuity condition. Accordingly, the function $g(z)$ used in this study is chosen as $g(z) = 2sinc(2z/b) - sinc(z/b)$ and $|z| < b$ region of the function is shown in Figure 2.1. The value of b is related with the dimension of the coil in the z-direction.

Fourier transform of the gradient field $B_z^{(m)}(c,k)$ is proportional with the function $\bar{g}(k)$ as given in (2.2). The Fourier transform of the $g(z)$ function used in this study is shown in Figure 2.2. As $b \to \infty$, the function $g(z)$ approaches to 1,

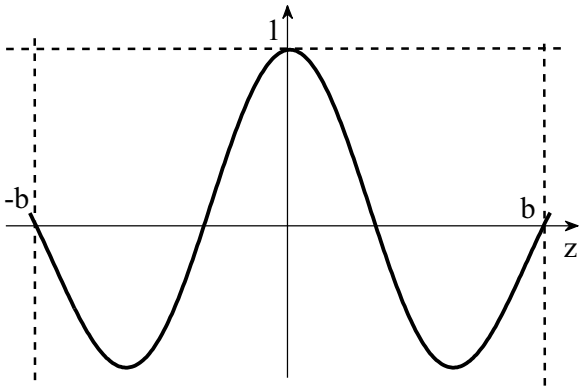

Figure 2.1: The specified $g(z)$ field.

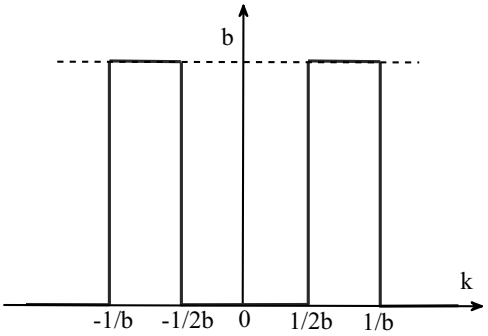

Figure 2.2: The Fourier transform of the specified $g(z)$ field. As $b \to \infty$, two pulses approach impulses at 0_+ and 0_-. However, $\bar{g}(k)$ remains equal to zero at $k = 0$.

in other words the gradient coil becomes infinitely long. On the other hand, $\bar{g}(k)$ approaches to two impulses at the left and right of zero while keeping its value zero at $k = 0$. Therefore, $\lim_{b\to\infty} \int_{-\infty}^{\infty} \bar{g}(k) f(k) dk = 1/2[\lim_{k\to 0^-} f(k) + \lim_{k\to 0^+} f(k)]$. When left and right limits are equal to each other, $\lim_{b\to\infty} \int_{-\infty}^{\infty} \bar{g}(k) f(k) dk = \lim_{k\to 0} f(k)$. Accordingly, the field equations can be simplified as follows:

$$
\begin{aligned}
E_\rho(\rho,\phi,z) &= -i\omega c G_x \sin\phi \Big[\lim_{k\to 0} e^{ikz} \frac{1}{k^2 I_1(kc)} \Big(\frac{I_1(k\rho)}{\rho} - \frac{I_1(k\rho_0) I_1'(k\rho)}{\rho_0 I_1'(k\rho_0)} \Big) \Big] \\
&= -i\omega G_x \sin\phi \Big(\frac{{\rho_0}^2 - \rho^2}{4} \Big), \qquad (2.9) \\
E_\phi(\rho,\phi,z) &= -i\omega c G_x \cos\phi \Big[\lim_{k\to 0} e^{ikz} \frac{1}{k I_1(kc)} \Big(I_1'(k\rho) - \frac{I_1(k\rho_0) I_1(k\rho)}{k^2 \rho_0 \rho I_1'(k\rho_0)} \Big) \Big] \\
&= -i\omega G_x \cos\phi \Big(\frac{{\rho_0}^2 + \rho^2}{4} \Big), \qquad (2.10)
\end{aligned}
$$

$$
\begin{aligned}
E_z(\rho,\phi,z) &= -\omega c G_x \sin\phi \Big[\lim_{k\to 0} e^{ikz} \frac{I_1(k\rho_0) I_1(k\rho)}{k^2 \rho_0 I_1'(k\rho_0) I_1(kc)} \Big] \\
&= -i\omega G_x \sin\phi \rho z, \qquad (2.11) \\
B_\rho(\rho,\phi,z) &= -iG_x c cos(\phi) \Big[\lim_{k\to 0} e^{ikz} \frac{I_1'(k\rho)}{I_1(kc)} \Big] \\
&= G_x z \cos\phi, \qquad (2.12) \\
B_\phi(\rho,\phi,z) &= iG_x c sin(\phi) \Big[\lim_{k\to 0} e^{ikz} \frac{I_1(k\rho)}{k\rho I_1(kc)} \Big] \\
&= -G_x z \sin\phi. \qquad (2.13)
\end{aligned}
$$

In the derivation of Eqs. (2.9)-(2.13), derivatives of the modified Bessel functions are substituted with the appropriate recurrence relations for the modified Bessel functions [32]. Additionally, in order to simplify the limit operation, small argument approximation for the Bessel functions is used. Note that since the electric field components vanish with the first order small argument approximation, the second order approximation is used for simplifications. For y- and z-gradient coils, target fields are defined as $B_z(c,\phi,z) = G_y c \sin\phi g(z)$ and $B_z(c,\phi,z) = G_z z g(z)$, respectively. The field expressions for these gradient coils are also simplified in the same way applied to the x-gradient coil. The resultant electric and magnetic field expressions in the Cartesian coordinates, in time domain are obtained as follows [33]:

$$
\begin{aligned}
E_x &= \frac{xy}{2}\frac{dG_x}{dt} + \frac{\rho_0^2 - x^2 + y^2}{4}\frac{dG_y}{dt} + \frac{yz}{2}\frac{dG_z}{dt}, \qquad (2.14) \\
E_y &= \frac{-\rho_0^2 - x^2 + y^2}{4}\frac{dG_x}{dt} - \frac{xy}{2}\frac{dG_y}{dt} - \frac{xz}{2}\frac{dG_z}{dt}, \qquad (2.15) \\
E_z &= -yz\frac{dG_x}{dt} + xz\frac{dG_y}{dt}, \qquad (2.16) \\
B_x &= zG_x - \frac{x}{2}G_z, \qquad (2.17) \\
B_y &= zG_y - \frac{y}{2}G_z, \qquad (2.18) \\
B_z &= xG_x + yG_y + zG_z. \qquad (2.19)
\end{aligned}
$$

Note that Eqs. (2.14)-(2.19) are obtained for a homogeneous cylindrical volume with the assumption that the gradient coil is infinitely long.

With these simplified electric field expressions, the induced voltage on the

implant lead can be calculated approximately by integrating tangential E field over the length of the lead.

2.4 Experimental Results

2.4.1 Experimental Setup

In this study, both phantom and ex vivo experiments are performed with a Siemens Magnetom TimTrio $3T$ system. In both experiments a fixed MRI sequence is applied and the changes are observed. In the MRI sequence, no RF pulses are used. The magnitude of the gradient pulses is set to $30mTm^{-1}$ with a ramp up and down time of $170\mu s$. The pulse duration is set to $5ms$. In the sequence, there is a $5ms$ gap between each gradient pulse. In phantom experiments, the implant is aligned along the z axis and the x axis in order to verify the accuracy of the equations for the field variations in the x and z-directions. 40 different implant lead positions along the z-axis are considered for the ex vivo experiments. x, y, and z positions of the leads are determined using the MR magnitude images. Approximate induced potential on the lead is computed theoretically by integrating tangential E field over the lead according to the position data.

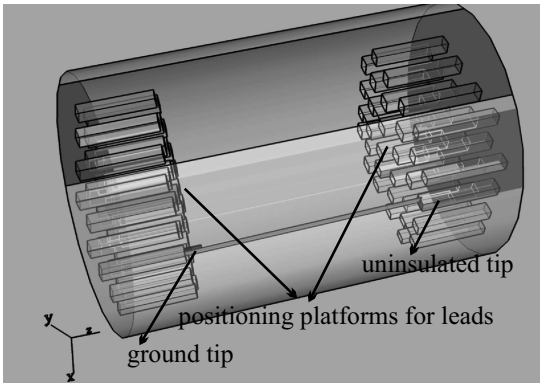

Figure 2.3: A cylindrical plexiglass phantom with a diameter of $30cm$ and a length of $50cm$ and the positioning of the lead.

Figure 2.3 illustrates the cylindrical plexiglass phantom with a diameter of $30cm$ and a length of $50cm$ used in the experiments. Wires acting as an implant lead are fixed at different positions in the phantom as shown in Figure 2.3. The diameter of the wire is $0.8mm$. The wires are insulated without shielding. One tip of the wire is left uninsulated and the other tip going out from the phantom is connected to an oscilloscope probe. There is another wire attached to this wire that acts as a ground which is taken as a reference level. As an oscilloscope, Agilent InfiniiVision $DSO7032A$ is used.

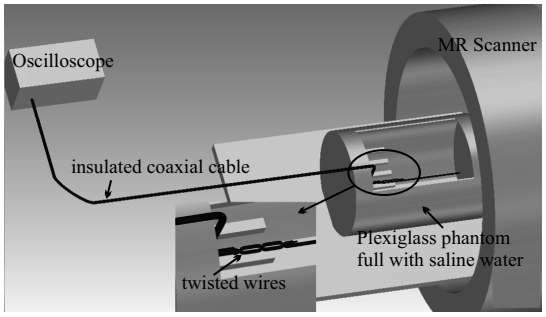

Figure 2.4: Experimental setup: Position of the wires, phantom and the oscilloscope.

The voltage is carried by insulated coaxial cable to the oscilloscope. Insulated wire outside the phantom is twisted in order to ensure that the measurement is only coming from the lead inside the phantom. The experimental setup is shown in Figure 2.4. For different implant lead positions, MR images of the phantom are taken and the signal waveform observed from the oscilloscope is stored. For each lead position, the peak voltage values observed in the oscilloscope are compared with theoretically computed voltage values for the respective lead positions.

A model of the ex vivo experiment setup is shown in Figure 2.5. These experiments are performed using the sciatic nerves of frogs. The nerve is kept alive inside Ringer's solution. One tip of a wire is soldered to a piece of copper plate, this plate emulates the pulse generator when there is no electrical component between the case and the lead, in other words when there is a short circuit between the case and the lead. The other tip of the wire touches the sciatic nerve of the frog as shown in Figure 2.5. Only the tip touching the nerve is left uninsulated (emulates the electrode). The same cylinder used in phantom

experiments is filled with Ringer's solution instead of saline water, and the frog leg and the wire are fixed inside the phantom.

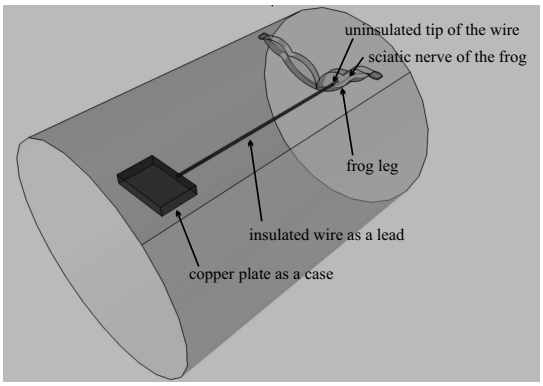

Figure 2.5: Location of the frog leg and the lead inside the phantom.

To determine the threshold voltage value that stimulates the frog nerve, the same signal waveform observed during the phantom experiments is generated with two signal generators outside the MR scanner. The voltage is applied to the nerve with the same insulated wire used in the experiments. By changing only the amplitude of the signal, the minimum voltage value that stimulates the nerve (i.e., the minimum voltage value at which a muscular contraction is observed visually) is determined and defined as the threshold voltage value. In the experiments under MR scanner for different implant lead positions, the stimulation of the frog nerve is observed visually. For each implant lead position, with the help of the MR images, the induced voltage values are computed and compared with the threshold voltage.

2.4.2 Results and Discussion

By using MATLAB (Mathworks, Natick, MA, USA), the electric field distributions are obtained by solving the simplified field expressions for an x-gradient coil with a diameter of $0.65m$, $20mTm^{-1}$ gradient magnitude and $100Tm^{-1}s^{-1}$ gradient switching rate, which are same as the parameters used in [27]. Figure 2.6 shows these electric field distributions for a conducting cylinder with $0.195m$ radius.

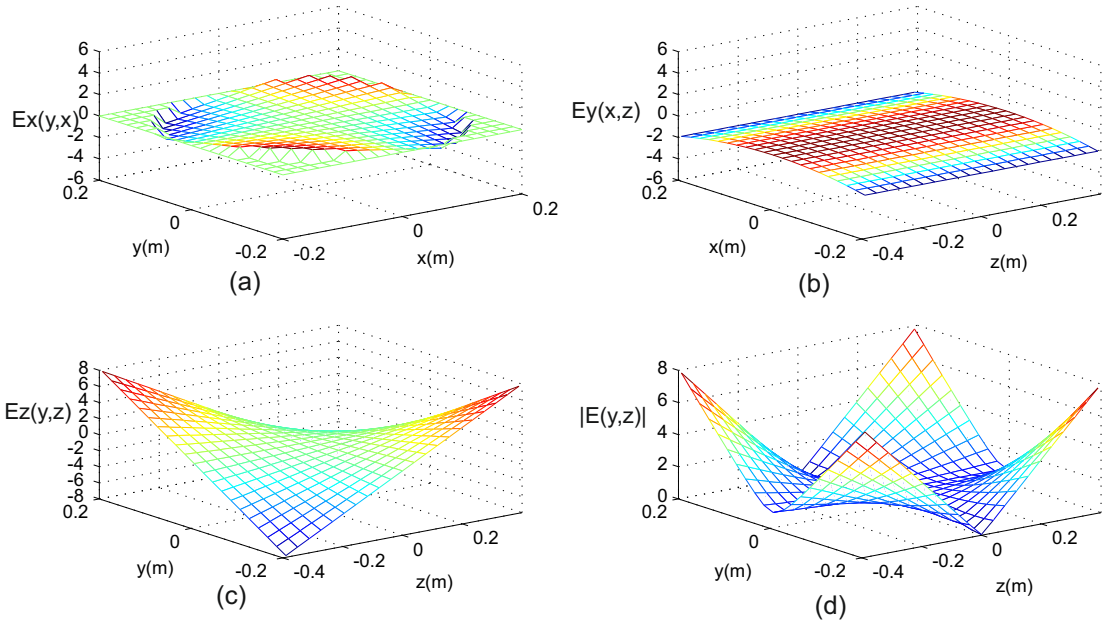

Figure 2.6: E-field distribution formed by the equation of our study for x-gradient coil. (a) $E_x(y, x)$ for $z = 0$. (b) $E_y(x, z)$ for $y = 0$. (c) $E_z(y, z)$ for $x = 0$. (d) $|E(y, z)|$ for $x = 0$.

In the linear region of the gradient field, the obtained field patterns show similar characteristics with those given in [27]. In [27], the peak value of $|E|$ for the x- coil with a gradient switching rate of $100Tm^{-1}s^{-1}$ is calculated as $5.25V/m$, whereas at the same location, this value is found to be $6.3V/m$ using the simplified expressions. In [3], this peak value is calculated as $4.2V/m$. For the z- coil, the peak value of $|E|$ is calculated as $4V/m$ in our study and in [27] it is $3.53V/m$.

In the phantom experiments, the measured voltage value for each lead position is compared with the analytically computed voltage values. Figure 2.7(a) shows the comparison of the calculated and the measured voltage values when the x-gradient coil is active and the implant leads are aligned in the z axis along the body. Figure 2.7(b) shows the same comparison for the activation of y-gradient coil. Unity line is shown to indicate the difference between the expected and the measured values.

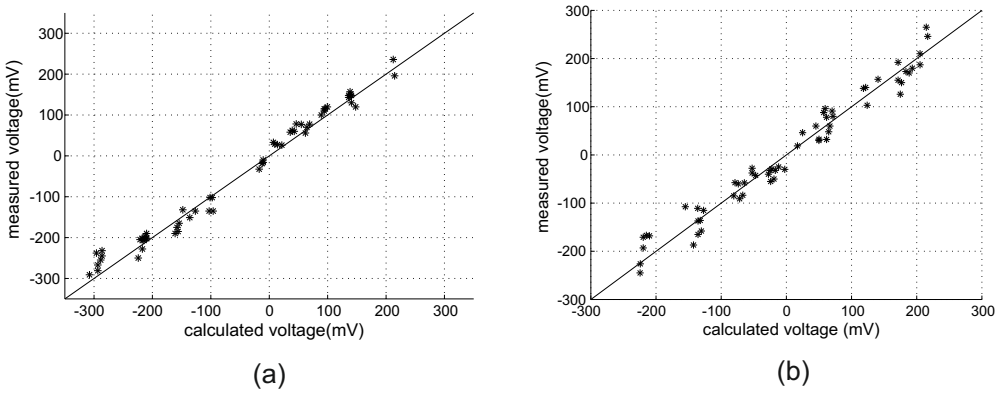

Figure 2.7: Comparison of the calculated and the measured voltage values for the activation of: (a) x-gradient coil, (b) y-gradient coil. (Note that implant leads are aligned in the z axis along the body)

According to these results, when the lead is aligned along the z-direction, the root-mean-square error between the calculated and the measured voltages is calculated as $26mV$. The error may be due to the fact that in the course of deriving the analytical expressions, both the gradient coils and the phantom are assumed to be infinitely long. However, the lengths are obviously finite in the experiments. For the z-gradient coil, the simplified field expressions show that E_z is expected to be zero. In the measurements, for the z-gradient coil, the voltage level is in $5 - 10mV$ range and noisy, so it is classified as an error.

Figure 2.8 shows the comparison of the calculated and the measured voltage values when z, y, and x-gradient coils are active, respectively and the implant leads are aligned in the x axis along the body. According to these results when the lead is along the x-direction, the root-mean-square error is calculated as $25mV$. In order to verify that the provided expressions are independent from the conductivity, experiments are repeated for different conductivity values and measurements at the same lead positions are noted. For these experiments, conductivity values are measured as $0.074S/m$, $0.25S/m$, $0.35S/m$, and $0.44S/m$. For 5 different lead positions, similar measurement results are obtained with a $3mV$ root mean square error. Note that in this study the analytical calculations

and the experiments are done for only a homogeneous body model and no comparison is given between homogeneous and heterogeneous body models unlike the experiments in [3]. However, if the field calculations cannot be done for each patient specifically, there will always be calculation errors, therefore simplified expressions may suffice to obtain approximate values to assess the stimulation risk.

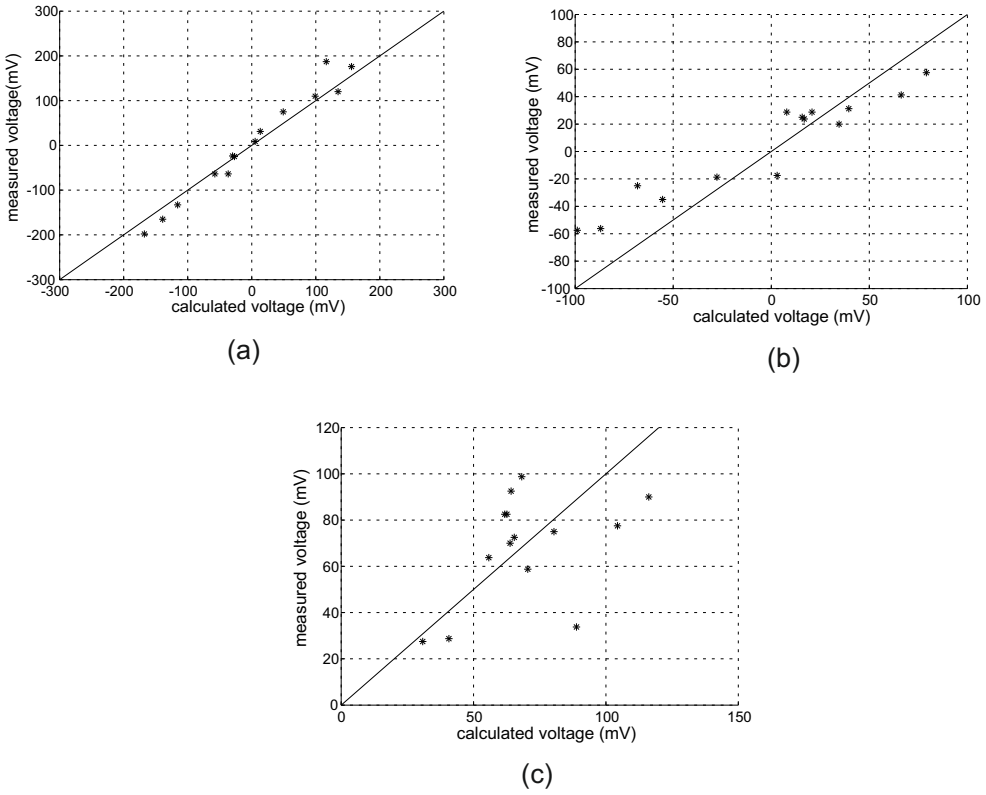

Figure 2.8: Comparison of the calculated and measured voltage values for the activation of: (a) z-gradient coil, (b) y-gradient coil, (c) x-gradient coil. (Note that implant leads are aligned in the x axis along the body)

In ex vivo experiments, 6 frogs are used and the stimulation risk is observed at 40 different lead positions. The threshold voltage value for stimulating the frog nerve is measured as $0.1V$ outside of the MR scanner. During MR experiments, coordinates of each lead position is determined by MR images, and for each case the approximate induced voltage values are calculated for x-, y- and z-gradient coils. It is seen that for 24 lead positions the calculated voltage values are between

$0.11V$ and $0.3V$. These values are bigger than the measured threshold voltage and stimulation is observed at these lead positions as expected. For the remaining 16 lead positions, the calculated voltage values are between $0.01V$ and $0.098V$. These values are smaller than the measured threshold voltage; hence, stimulation is not expected. However, in the two lead positions where the calculated voltages are $0.094V$ and $0.098V$, stimulation is also observed. Therefore, we decided to set an approximate threshold voltage level as $0.09V$ allowing a 10% difference with the measured one. Note that this 10% difference can be attributed to $5 - 10mV$ error margin as mentioned before. A similar difference is also observed in phantom experiments where the measured voltages are slightly higher than the calculated ones for some lead locations.

The error in these simplified expressions needs to be investigated for non cylindrical and heterogeneous objects like human body. Furthermore, in this work we assumed that the implantable pulse generator (IPG) case is directly connected to the lead. Although this may be considered as a worst case condition, the impedance between the lead and the IPG and the other circuit elements (e.g. EMI capacitors) used to enhance the MRI compatibility of the AIMD can also be put into the model and with this model gradient induced current passing through the lead can be calculated with the knowledge of the induced voltage. This analysis with experimental verifications is planned as a future study.

2.5 Conclusion

In this study we derived simplified expressions for the electric field inside the cylindrical homogeneous body model for a perfectly uniform gradient field. These simple expressions may be used to understand the nerve stimulation risk when there is an implant. Both phantom and ex vivo experiments are performed and results show that if the path of the implant lead is known, the induced voltage on the lead can be estimated analytically.

Chapter 3

An Approximate Fourier Domain Expression for Bloch-Siegert Shift

3.1 Preface

This chapter is based on an article that is submitted to Magnetic resonance in Medicine. The content of this chapter was presented in part at the Scientic Meetings of International Society of Magnetic Resonance in Medicine in 2012 and 2013 [15, 16].

3.2 Introduction

The Bloch-Siegert (BS) based B_1 mapping technique was proposed by Sacolick [17] as a phase-based B_1 mapping technique. This technique utilizes the fact that applying an off-resonance RF field after an excitation RF adds phase to the excited spins and for a large off-resonance frequency, the added phase is

directly proportional to the square of the B_1 field magnitude [34]. This technique is insensitive to spin relaxation, repetition time (TR), starting flip angle, chemical shift, and B_0 field inhomogeneities. However, this technique has some limitations. For example, the sequence has a long echo time (TE) compared to a standard sequence without BS pulses. Furthermore the sequence causes high Specific Absorption Rate (SAR) due to the relatively long off-resonant RF pulse used to create the BS phase shift.

To improve this technique, there have been studies on the optimization of the sequence and the off-resonant RF pulse shape [35–41]. In [35], the BS pulse shape was optimized to both maximize the sensitivity of the measurement of B_1 magnitude for given SAR and T2 values and also to decrease TE and SAR values. In the same study, the authors also mentioned that crusher gradients were added before and after a BS pulse to minimize the artifacts due to on-resonant excitation by the BS pulse. In [36], an adiabatic RF pulse design was introduced to increase the sensitivity of the measurement of $|B_1|$. In [37], a faster acquisition of the B_1 information and a minimized signal loss due to $T2^*$ effects were achieved. In [38], a new sequence that caused a lower SAR than that of a spin echo sequence with a similar signal-to-noise ratio (SNR) was proposed. In [39], a new sequence with an optimized BS pulse and echo-planar and spiral readouts was used to reduce SAR and improve the scan efficiency. In [40], an algorithm to design an optimized BS pulse was proposed and with the experiments it was shown that better phase sensitivity can be obtained in a shorter time and with lower on-resonance excitation than the Fermi pulse with designed pulses. In [41], reducing the off-resonance frequency to improve the sensitivity of the BS based B_1 mapping method was proposed. In the same study, the effects of the crusher gradients were also discussed. All of these studies improve the weaknesses of the BS based B_1 mapping technique by modifying the sequence or the RF pulse shape.

In this study, our aim is to describe the parameters that affect the BS based B_1 mapping method and to investigate the relationship between the effects of the off-resonance frequency, the RF pulse shape, and the duration of the RF pulse. To this end, we propose a general expression based on theoretical modeling that

relates the Fourier transform of the off-resonant BS RF pulse envelope to the phase shift. To verify the accuracy of the proposed expression, we conducted extensive simulations and experiments. These simulations and experiments show that the proposed frequency domain expression is more accurate than the time domain expression that was proposed by the authors of the BS shift based B_1 mapping method [17].

3.3 Theory

In the BS Shift based B_1 mapping method, an off-resonant RF pulse is applied after an excitation RF pulse to add a phase shift to the excited spins. The amount of phase shift (ϕ_{BS}) depends on both the applied RF field ($B_1^+(t)$) and on the frequency offset of the RF pulse ($\omega_{RF}(t)$) from the resonance frequency (ω_0) [34, 42]. In [17], it has been shown that if $\omega_{RF}(t)$ is much higher than $|\omega_1(t)| = \gamma|B_1^+(t)|$, where γ is the gyromagnetic ratio, then in the ω_0 rotating frame the phase shift is directly related to the time integral of the square of $|\omega_1(t)|$, as given in Eq. (3.1):

$$\phi_{BS} \approx \phi_{TD} = \int_0^T \omega_{TD}(t)\mathrm{d}t. \tag{3.1}$$

where $\omega_{TD}(t) = \frac{|\omega_1(t)|^2}{2\omega_{RF}(t)}$.

Because long Bloch-Siegert pulse durations cause long TE values, which results in signal loss due to the $T2^*$ and $T2$ effects, the use of a small pulse duration becomes important. However, as our preliminary results have shown [33], when a small pulse duration is used, for the same peak $|B_1|$ value, there is a significant difference between the actual phase shift (ϕ_{BS}), as obtained by the solution of the complete Bloch equations, and the phase shift given by Eq. (3.1), even if the condition $\omega_{RF}(t) >> |\omega_1(t)|$ is satisfied. This difference (ϕ_{res}) is defined as:

$$\phi_{res} = \phi_{BS} - \phi_{TD}. \tag{3.2}$$

In fact, ϕ_{res} can be directly obtained if the Bloch equations are solved in the $\omega_0 + \omega_{TD}(t)$ rotating frame, because by doing so, the phase accumulation due to $\omega_{TD}(t)$ is excluded from the actual phase shift in the ω_0 rotating frame. (Note that this rotating frame is named as BS time domain (BSTD) rotating frame.) In BSTD rotating frame, $B_1^+(t)$ is defined as:

$$B_1^+(t) = B_1^e(t) exp\Big[i\Big(\int_0^t (\omega_{RF}(\tau) - \omega_{TD}(\tau))\mathrm{d}\tau + \theta + \theta_0\Big)\Big], \tag{3.3}$$

where $B_1^e(t)$ is the envelope, θ is the phase of the applied Bloch-Siegert shift RF pulse, and θ_0 is the accumulated phase until the beginning of the BS pulse.

The Bloch equation in matrix form in the BSTD rotating frame is given as:

$$\frac{d}{dt}\begin{pmatrix} M_x \\ M_y \\ M_z \end{pmatrix} = \begin{pmatrix} 0 & -\omega_{TD}(t) & -\omega_{1y}(t) \\ \omega_{TD}(t) & 0 & \omega_{1x}(t) \\ \omega_{1y}(t) & -\omega_{1x}(t) & 0 \end{pmatrix} \begin{pmatrix} M_x \\ M_y \\ M_z \end{pmatrix} \tag{3.4}$$

where $\omega_{1x}(t)$ and $\omega_{1y}(t)$ are the real and imaginary parts of $\omega_1(t)$, respectively as follows:

$$\omega_{1x}(t) = \gamma B_1^e(t) \cos\Big(\int_0^t (\omega_{RF}(\tau) - \omega_{TD}(\tau))\mathrm{d}\tau + \theta + \theta_0\Big), \tag{3.5}$$

$$\omega_{1y}(t) = \gamma B_1^e(t) \sin\Big(\int_0^t (\omega_{RF}(\tau) - \omega_{TD}(\tau))\mathrm{d}\tau + \theta + \theta_0\Big). \tag{3.6}$$

In the BSTD rotating frame, the magnetization vector at time zero (the time that BS RF pulse is started) is $M(0) = (M_0\ 0\ 0)^T$, where T stands for the vector transpose. Under this condition, the time derivative of M_x is very small, and it is assumed that M_x remains almost constant throughout the Bloch-Siegert RF pulse. Therefore the system of differential equations is reduced to:

$$\frac{d}{dt}\begin{pmatrix} M_y \\ M_z \end{pmatrix} = \begin{pmatrix} 0 & \omega_{1x}(t) \\ -\omega_{1x}(t) & 0 \end{pmatrix} \begin{pmatrix} M_y \\ M_z \end{pmatrix} + \begin{pmatrix} \omega_{TD} \\ \omega_{1y}(t) \end{pmatrix} M_0. \tag{3.7}$$

Eq. (3.7) is rewritten for M_y and M_z magnetization components as the following:

$$\frac{d}{dt}M_y(t) = \omega_{1x}(t)M_z(t) + \omega_{TD}M_0, \tag{3.8}$$

$$\frac{d}{dt}M_z(t) = -\omega_{1x}(t)M_y(t) + \omega_{1y}(t)M_0. \tag{3.9}$$

Note that $\omega_{1x} = \gamma B_1^e(t)\cos(\int_0^T(\omega_{RF}(t) - \omega_{TD})\mathrm{d}t + \theta + \theta_0)$ and $\omega_{1y} = \gamma B_1^e(t)\sin(\int_0^T(\omega_{RF}(t) - \omega_{TD})\mathrm{d}t + \theta + \theta_0)$. These differential equations are written as a single differential equation in the form of M_{yz} where $M_{yz} = M_y + iM_z$

$$\frac{d}{dt}M_{yz}(t) = -i\omega_{1x}(t)M_{yz}(t) + \Big(\omega_{TD} + i\omega_{1y}(t)\Big)M_0. \tag{3.10}$$

The solution of this first order differential equation can be written as:

$$M_{yz}(t) = f(t)exp\Big(-i\int_0^t \omega_{1x}(s)\mathrm{d}s\Big). \tag{3.11}$$

To find $f(t)$, this solution is plugged into Eq. (3.10) As a result, the solution for M_{yz} at time T is found to be the following.

$$M_{yz}(T) = M_0\int_0^T \Big(\omega_{TD} + i\omega_{1y}(t)\Big)exp\Big(-i\int_t^T \omega_{1x}(s)\mathrm{d}s\Big)\mathrm{d}t. \tag{3.12}$$

To simplify the solution, the exponential term is simplified by using the fact that $\omega_{RF}(t) >> |\omega_1(t)|$ because $\omega_{1x}(s)$ is a sinusoidal function and the integration result only becomes maximum during its one cycle, which gives $\frac{2\gamma|B_1^e|}{\omega_{RF}}$, when $B_1^e(t)$ is a slowly varying function compared to $\omega_{RF}(t)$. Therefore :

$$exp\Big(-i\int_t^T \omega_{1x}(s)\mathrm{d}s\Big) \approx 1 - i\int_t^T \omega_{1x}(s)\mathrm{d}s, \tag{3.13}$$

With this simplification, the solution can easily be separated into its real and imaginary parts, and the components M_y and M_z can be obtained as:

$$M_y(T) \approx M_0 \int_0^T \omega_{TD}(t)\mathrm{d}t + M_0 \int_0^T \int_t^T \omega_{1y}(t)\omega_{1x}(s)\mathrm{d}s\mathrm{d}t, \tag{3.14}$$

$$M_z(T) \approx M_0 \int_0^T \omega_{1y}(t)dt - M_0 \int_0^T \int_t^T \omega_{TD}(t)\omega_{1x}(s)\mathrm{d}s\mathrm{d}t. \tag{3.15}$$

Because we assume that $M_x(T) = M_0$ and $M_y(T)$ are small, a phase can be found as $\phi = -tan^{-1}\frac{M_y(T)}{M_0} \approx -\frac{M_y(T)}{M_0}$ (note that the minus sign is due to the fact that the phase is defined in left-hand direction), and the expression for ϕ_{res} in BSTD rotating frame becomes:

$$\phi_{res} \approx -\int_0^T \int_t^T \omega_{1y}(t)\omega_{1x}(s)\mathrm{d}s\mathrm{d}t - \int_0^T \omega_{TD}(t)dt \tag{3.16}$$

To find the phase shift defined in the ω_0 rotating frame, which is the actual phase shift, we add the term ϕ_{TD} to ϕ_{res} as given in Eq. (3.2). Note that the term θ_0, which is the phase accumulated prior to the beginning of the BS pulse, is also subtracted to get the phase shift in the ω_0 rotating frame:

$$\phi_{BS} \approx -\int_0^T \int_t^T \omega_{1y}(t)\omega_{1x}(s)\mathrm{d}s\mathrm{d}t - \theta_0 \tag{3.17}$$

Because the contribution of θ_0 is canceled by using the difference of two acquisitions taken with positive and negative offset frequencies, it is ignored in the rest of the equations. Note that $\omega_{1x}(s)$ and $\omega_{1y}(t)$ remain the same values as defined in BSTD frame.

To find a simplified solution for ϕ_{BS}, the limits of the integration are changed by adding a unit step function ($u(t)$) as follows:

$$\phi_{BS} \approx -\int_0^T \int_0^T \omega_{1y}(t)\omega_{1x}(s)u(s-t)\mathrm{d}s\mathrm{d}t. \tag{3.18}$$

$\omega_{1x}(t)$ and $\omega_{1y}(t)$ are expressed in terms of $\omega_1(t)$ and $\omega_1^*(t)$, where $\omega_1^*(t)$ is the complex conjugate of $\omega_1(t)$, and Eq. (3.18) is rewritten in terms of $\omega_1(t)$ and $\omega_1(t)^*$ as the following:

$$\phi_{BS} \approx -\int_0^T \int_0^T \frac{\omega_1(t) - \omega_1^*(t)}{2i} \times \frac{\omega_1(s) + \omega_1^*(s)}{2} u(s-t) \mathrm{d}s\mathrm{d}t. \tag{3.19}$$

To obtain a Fourier relation instead of a $\omega_1(t)$ term, we used the Fourier relation $\int_{-\infty}^{\infty} \Omega_1(f_t) exp(i2\pi f_t t) \mathrm{d}f_t$ as follows:

$$\phi_{BS} \approx -\int_0^T \int_0^T \int_{-\infty}^{\infty} \int_{-\infty}^{\infty} \frac{\Omega_1(f_t) - \Omega_1^*(-f_t)}{2i} e^{i2\pi f_t t} \frac{\Omega_1(f_s) + \Omega_1^*(-f_s)}{2} e^{i2\pi f_s s} u(s-t) \mathrm{d}f_s \mathrm{d}f_t \mathrm{d}s\mathrm{d}t. \tag{3.20}$$

The variables t and s are replaced with the new variables q and r, where $s = (r+q)/\sqrt{2}$ and $t = (q-r)/\sqrt{2}$. By changing the order of the integrals and using the relation:

$$\int_{-\infty}^{\infty} u(\sqrt{2}r) e^{(i2\pi f_r r)} \mathrm{d}r = -\Big(\frac{1}{2}\delta(f_r) + \frac{1}{i2\pi f_r}\Big) \tag{3.21}$$

the final expression becomes the following:

$$\phi_{BS} \approx -\int_{-\infty}^{\infty} \frac{|\Omega_1(f)|^2}{4\pi f} df - \frac{\Omega_1^2(0) - \Omega_1^* 2(0)}{8i} \tag{3.22}$$

Because $\omega_1(t)$ is defined in a BSTD rotating frame, ($\omega_0 + \omega_{TF}$ rotating frame) such as;

$$\omega_1(t) = \gamma B_1^e(t) exp\Big[i\Big(\int_0^t (\omega_{RF}(\tau) - \omega_{TD}) \mathrm{d}\tau\Big)\Big] exp(i(\theta + \theta_0)), \tag{3.23}$$

the term $e^{i(\theta+\theta_0)}$ stands out in the $\Omega_1(f)$ term. The second part of Eq. (3.22) also includes these phase terms. On the other hand, because the phase difference of two acquisitions taken with positive and negative offset frequencies is used and the term $e^{i(\theta+\theta_0)}$ does not change, we can ignore this part. So, the expression simplifies to the following relation:

$$\phi_{BS} \approx -\int_{-\infty}^{\infty} \frac{|\Omega_1(f)|^2}{4\pi f} \mathrm{d}f \tag{3.24}$$

This expression is simplified by using the Hilbert transform. The Hilbert transform of a function is defined as $Hg(t) = \frac{1}{\pi}\int_{-\infty}^{-\infty}\frac{g(\tau)}{t-\tau}\mathrm{d}\tau$. The Hilbert transform is defined as the Cauchy principal value of the integral in this equality whenever the value of the integral around the pole $t = \tau$ exists. The Cauchy principal value is obtained by considering a finite range of integration that is symmetric about the point of singularity and the region with the singularity is excluded. While the interval of the integral approaches ∞, the length of the excluded interval approaches zero. The Hilbert transform of $g(t)$ at $t = 0$ can be expressed as $Hg(0) = -\frac{1}{\pi}\int_{-\infty}^{-\infty}\frac{g(\tau)}{\tau}\mathrm{d}\tau$. With this information, the Fourier domain approximation of the Bloch-Siegert shift becomes the following:

$$\phi_{BS} \approx \phi_{FD} = -\int_{-\infty}^{\infty}\frac{|\Omega_1(f)|^2}{4\pi f}df = \frac{H|\Omega_1|^2(0)}{4} \tag{3.25}$$

To find the peak of the B_1 field from the phase in $\omega_{RF}(t) >> |\omega_1(t)|$ region Eq. (3.25) is changed to the following equation:

$$B_{1peak} \approx \frac{1}{\gamma}\sqrt{\frac{4\phi_{FD}}{H|\Omega_{norm}|^2(0)}} \tag{3.26}$$

where $\Omega_1(f) = \gamma B_{1peak}\Omega_{norm}(f)$.

As an example, Eq. (3.25) is analytically solved for a hard pulse with a pulse duration (T) and constant offset frequency (ω_{RF}) in $\omega_{RF}(t) >> |\omega_1(t)|$. The resultant expression becomes as the following:

$$\phi_{FD} = \frac{(\gamma B_{1peak})^2 T}{2(\omega_{RF})}\Big[1 - \mathrm{sinc}\Big(\frac{\omega_{\mathrm{RF}}}{\pi}\mathrm{T}\Big)\Big]. \tag{3.27}$$

Analysis of this new approximated frequency domain BS relation(Eq. (3.25)) for hard, Fermi and Shinner-Le Roux (SLR) pulse shapes and a comparison of the results with (i) the solution of the time domain approximated relation (Eq. (3.1)), (ii) the results of the Bloch simulations, and (iii) the results of the experiments are given in the following section.

3.4 Methods

To investigate the parameters that affect the Bloch-Siegert shift based B_1 mapping method and to verify Eq. (3.25) expressed in the theory section, Bloch simulations and MR experiments are performed for different pulse shapes. For the Bloch-Siegert B_1 mapping method, choosing the off-resonant RF pulse shape properly is critical because this affects the phase value, the minimum offset frequency that can be used, and the minimum undesired magnetization tilting effect. In [17], the hard, Fermi, adiabatic hyperbolic secant and the adiabatic tanh/tan pulses were compared in terms of their frequency range that contains 99% of spin excitation and the constant, K_{BS}, describing the phase shift. As a result, the Fermi pulse was chosen for the experiments. In our experiments, however, only hard, Fermi and SLR pulse shapes are used. The envelope of the Fermi pulse is defined by the expression $\frac{1}{1+e^{(|(t)|-t_0)/a}}$, where the parameters t_0 and a are defined as $T = 2t_0 + 13.81a$ and $t_0 = 10a$, and T is the pulse duration. The SLR pulse is designed with 0.5% passband ripple, 1% reject ripple and 0.3 kHz bandwidth by using VESPA-RFPulse tool [43]. In Figure 3.1, we present the pulse shapes and their frequency domain patterns. Pulse magnitudes are normalized in such a way that the same phase values can be obtained for an 8 ms pulse duration and a 4 kHz offset frequency.

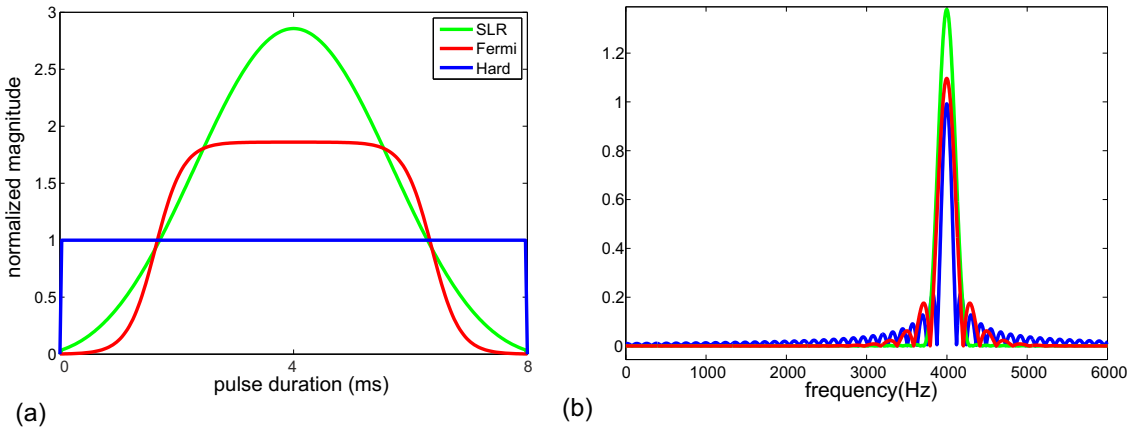

Figure 3.1: (a) Pulse shapes used in the analysis. (b) Fourier transforms of each pulse with a 4 kHz offset frequency and a 8 ms pulse duration.

The experiments were performed in the 3T scanner (MAGNETOM Trio a

Tim System, Siemens Healthcare, Erlangen, Germany) with a cylindrical 1900 ml Siemens phantom with 10 cm diameter (3.75% NISO4x6H2O + 5% NaCl). During the experiments, a FLASH sequence modified by adding an off-resonant pulse after the excitation RF was used. The excitation RF was a sinc pulse with a 1 ms duration. Crusher gradients with 1 ms duration in slice selection direction were added to the sequence before and after the off-resonant pulse [41], and the phase encoding gradient was applied before the off resonant RF pulse to avoid encoding the undesired off-slice spins that were excited by the off-resonant RF pulse. Figure 3.2 shows the modified sequence. In each experiment, two phase images were acquired by using a BS pulse with positive and negative offset frequencies, and phase shifts were calculated by taking the difference of these two phase images. For each experiment, imaging parameters were set to 150 ms TR, 5 mm slice thickness, 256×256 in-plane resolution, and 200 mm field of view (FOV). The $|B_1^+|$ value calculated by Eq. (3.1) using the phase shift obtained with a Fermi pulse with an 8 ms pulse duration and a $4kHz$ offset-frequency for a given RF voltage, is used to establish the calibration factor between the peak $|B_1^+|$ and the applied RF voltage level. For RF transmission and reception, a transmit/receive rectangular coil with 10×23 cm dimension and tuned by 8 capacitors was used. Note that the flip angle is space dependent due to the usage of the surface coil. Therefore, for each experiment, data has been collected from the same region with a maximum and constant B_1^+ field distribution.

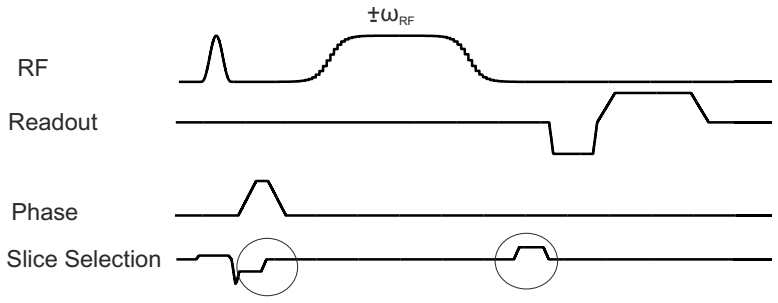

Figure 3.2: Pulse sequence used in the experiments. Crusher gradients (encircled by lines) are used to reduce out of slice effects.

While investigating the effect of the pulse duration through experiments and

simulations for hard and Fermi pulse shapes, the pulse duration was varied between 150 μs and $2ms$, with 50 μs steps, and the SLR pulse shape duration was varied between 300 μs and 2 ms, with 50 μs steps. TE values are set according to the BS pulse from 6.5 ms to 8.5 ms. The experiments were repeated 7 times for each pulse and pulse duration. The pulse duration versus phase plots were computed with the mean values and the standard deviation computed across the 7 repeats.

In the Bloch-Siegert shift based B_1 mapping technique, the sensitivity of the phase shift is inversely proportional to ω_{RF}, as seen in Eq. (3.1). To obtain a more accurate $|B_1^+|$ estimate one may prefer to decrease ω_{RF}. The maximum $|B_1^+|$ value that can be detected is then limited by the requirement $\omega_{RF} >> |\omega_1(t)|$. To understand the relation between the phase and the off-resonance frequency and to compare the results of frequency domain approximation (Eq. (3.25)) and time domain approximation (Eq. (3.1)), the results of the simulations and experiments for different offset frequencies were investigated. For this analysis, hard, Fermi, and SLR pulse shapes with an 8 ms pulse duration were used. The TE value was set to 14.5 ms in these experiments. According to the reference $|B_1^+|$ value obtained with a Fermi pulse with an 8 ms pulse duration and a 4 kHz offset-frequency and by using the linear relation between the induced B_1 field and the applied voltage, the magnitudes of the B_1 fields were acquired and the phase shifts obtained at the same points on the phase image were noted for each applied voltage. This experiment was repeated for 100 Hz, 1 kHz and 4 kHz offset frequencies. The experiments were repeated 5 times for each pulse and offset frequency. The B_1^+ versus phase plots were computed with the mean values and the standard deviation computed across the 5 repeats.

To correct for the effect of the B_0 offset frequency in the simulations, especially for small offset frequencies, B_0 maps were obtained by using two gradient echo images with different echo times (i.e. $\nabla TE = 1\ ms$), while the other imaging parameters were kept constant.

For the simulations, the Bloch equations were solved numerically in MATLAB (Mathworks, Natick, MA, USA) by using rotation matrices in an ω_0 rotation

frame. The magnetization was described by three 10×10 matrices in x, y and z directions. The elements of the matrices were located at a distance of 1.56 mm from each other on the x-y plane. Initially magnetization in z-direction was one, and the magnetizations in x and y directions are zero. Crusher gradients were also added to the simulations.

3.5 Results

3.5.1 Effect of the Pulse Duration

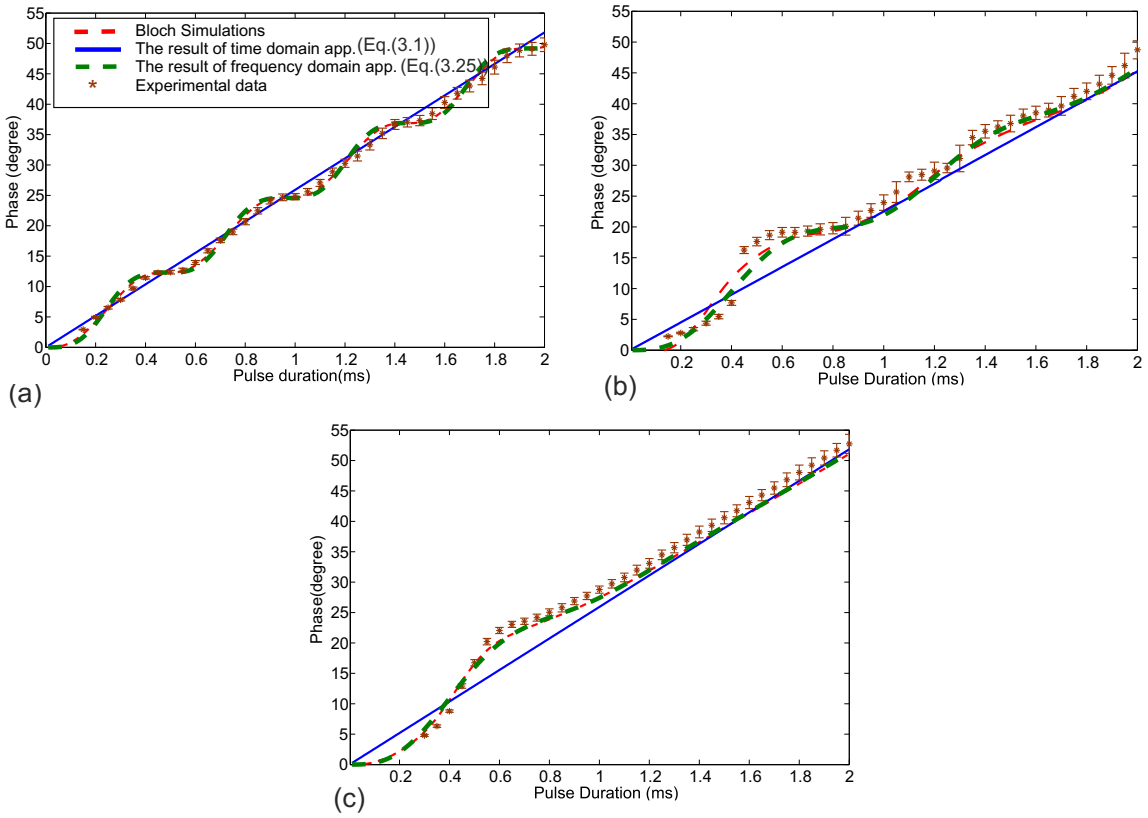

Figure 3.3: Phase difference for different pulse durations for (a) Hard, (b) Fermi, and (c) SLR pulses with a 2 kHz offset frequency.

In Figure 3.3, we present a comparison of the phase shifts obtained by simulations, by MR experiments, by applying Eq. (3.1), and by applying Eq. (3.25)

for different pulse durations and for hard, Fermi, and SLR pulse shapes with a 2 kHz offset frequency. From the applied voltages, the peak $|B_1^+|$ is estimated as 12.6 μT for the hard pulse, 16.2 μT for the Fermi pulse, and 21.1 μT for the SLR pulse, where $(\omega_1/\omega_{RF}) \leq 0.5$. These peak $|B_1^+|$ values were appropriate to obtain a similar range of phase shifts for hard, Fermi and SLR pulse shapes. As seen in the figure, the results of the experiments follow the results of the Bloch simulations. Furthermore, the phase shifts obtained by Eq. (3.25) and the phase shift obtained by the Bloch simulations exhibit a similar behavior in terms of both their dependence on pulse duration and their small differences. However, there is an appreciable difference between the results of Eq. (3.1) and the results of the simulations. This difference is more significant for Fermi and SLR pulses than the difference observed for the hard pulse. To compare the results quantitatively, the absolute maximum phase differences of closed form expressions ($\phi_{TD}$and ϕ_{FD}) relative to simulation and experimental results have been calculated. The absolute maximum phase differences between ϕ_{FD} and the Bloch simulations is less than 1 degree for all pulse shapes. However, for hard, Fermi and SLR pulse shapes, the absolute maximum phase differences between ϕ_{TD} and the Bloch simulations are 2.5 degrees, 4 degrees and 5 degrees at 0.6 ms pulse duration corresponding to 20%, 24% and 25% errors, respectively. Note that the absolute maximum phase differences between ϕ_{TD} and the experiments are around 6 degrees at 0.6 ms pulse duration for Fermi and SLR pulse shapes.

Figure 3.4 demonstrates the difference between the B_1 maps calculated by ϕ_{TD} and ϕ_{FD} expressions when a Fermi pulse with 0.6ms pulse duration and 2kHz offset frequency is used as a BS pulse. Unlike the previous experiments, body coil was used for transmission and 12 channel Siemens head coil was used for reception in these experiments. (Flip angle was set as 60°, FOV=200 mm, TR/TE=100ms/14.5ms (for BS pulse with 8ms pulse duration)-7ms (for BS pulse with 0.6ms pulse duration) and matrix=256×256.) Figure 3.4-(a) shows the reference B_1 map obtained by a Fermi pulse with 8ms pulse duration and 4kHz offset frequency. Note that for this reference map, both ϕ_{TD} and ϕ_{FD} approximations give the same results. When pulse duration and offset frequency are set to the lower values such as 0.6ms and 2kHz, respectively for the same RF voltage, the

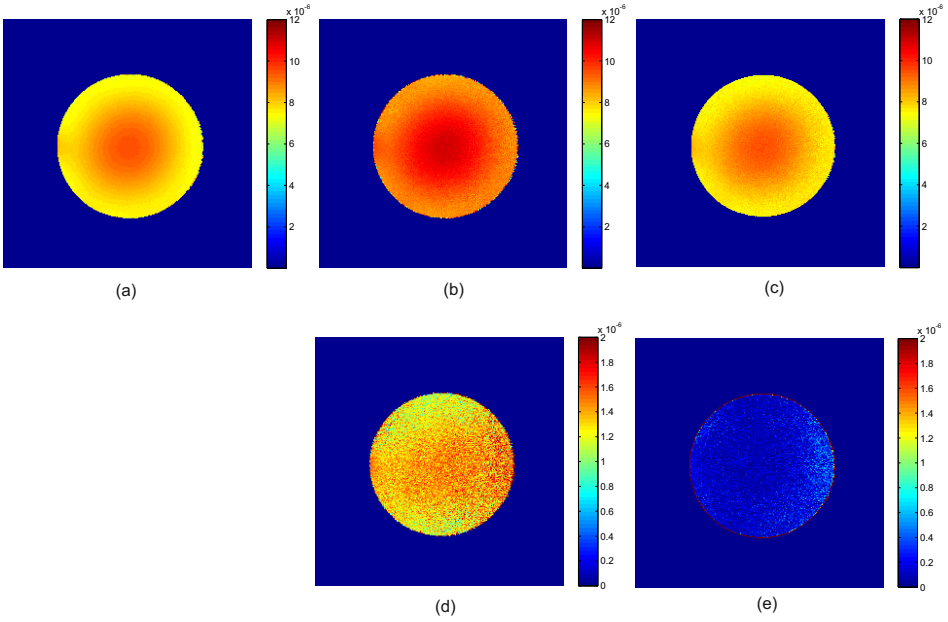

Figure 3.4: (a) Reference B_1 map (in terms of T) calculated with ϕ_{BS} relation ($\phi_{TD} \approx \phi_{FD}$) for a Fermi pulse with 8ms duration and 4kHz offset frequency where $(\omega_1/\omega_{RF}) \leq 0.1$, (b) B_1 map (in terms of T) calculated with ϕ_{TD} relation for a Fermi pulse with 0.6ms duration and 2kHz offset frequency where $(\omega_1/\omega_{RF}) \leq 0.2$, (c) B_1 map (in terms of T) calculated with ϕ_{FD} relation for a Fermi pulse with 0.6ms duration and 2kHz offset frequency where $(\omega_1/\omega_{RF}) \leq 0.2$, (d) Difference between the reference B_1 map and B_1 map calculated with ϕ_{TD} relation, (e) Difference between the reference B_1 map and B_1 map calculated with ϕ_{FD} relation.

difference between the reference B_1 map and the B_1 map calculated with ϕ_{TD} becomes significant as shown in Figure 3.4-(d).

3.5.2 Effect of the Off-Resonance Frequency

In Figure 3.5, we present a comparison of the phase shifts obtained through Bloch simulations, observed in the experiments, obtained by Eq. (3.1), and obtained by Eq. (3.25) for different B_1 magnitudes and offset frequencies. From the applied voltages, the excitation RF peak $|B_1^+|$ is estimated to be 29 μT. Although, at $1kHz$ and $4kHz$ frequencies, all results match very closely, when the offset

frequency is $100Hz$, the results of Eq. (3.1) start to deviate from the results of Bloch equations and from the results of experiments, whereas Eq. (3.25) gives closer results. It should be noted that at low offset frequencies, precise knowledge of the B_0 field and therefore, the B_0 frequency offset is critically important. In these experiments, the B_0 offset frequency was measured as 25 Hz, and this was taken into account during the simulations.

With the data shown in Figure 3.5, percent errors (i.e. $|\phi_{n1}-\phi_{n2}|/(\phi_{n1})\times 100$) between the results of the simulations and the results of Eq. (3.1) and also between the simulations and the results of Eq. (3.25) were calculated to investigate the accuracy of the equations in relation to the approximation $\omega_{RF} >> \omega_1$. The error for each pulse shapes was calculated as smaller than 3% at 4 kHz offset frequency for up to 29 μT B_1 values for which $(\omega_1/\omega_{RF}) \leq 0.3$ applies. For the Fermi pulse shape with 1 kHz offset frequency the error was smaller than 5 %, when $(\omega_1/\omega_{RF}) \leq 0.5$. For an SLR pulse shape with 1 kHz offset frequency, the error between the result of the simulations and the results of Eq. (3.1) was smaller than 5%, when $(\omega_1/\omega_{RF}) \leq 0.55$ and the error between the results of the simulations and the results of Eq. (3.25) was smaller than 5%, when $(\omega_1/\omega_{RF}) \leq 0.62$. For all of the pulse shapes with 100 Hz offset frequency, the error between the results of the simulations and the results of Eq. (3.1) was more than 8%, but the error between the results of the simulations and the results of Eq. (3.25) was less than 5%, when $(\omega_1/\omega_{RF}) \leq 0.55$.

In Figure 3.6, we demonstrate that there is a limitation for reducing the offset frequency to increase the phase. As seen in this figure, inverse proportionality between the phase and the offset frequency starts to become invalid after some frequency. This figure also shows that the results of the frequency domain approximation (ϕ_{FD}) follow the results of the simulations quite well for all the simulated frequency points, even though the time domain approximation (ϕ_{TD}) fails at lower offset frequencies.

Moreover, it can be argued that use of low offset frequencies may be counterproductive because the MR signal level may decrease due to on-resonance effects. In our experiments, it is observed that when the BS pulses with 100 Hz

offset frequency were used, the signal level decreased by up to 50% while $|B_1^+|$ increased from 0.5 μT to 5 μT. On the other hand, in the $|B_1|$ range for which $\omega_1/\omega_{RF} \leq 0.5$, there was a 10% decrease of the signal level. Therefore, when $\omega_1/\omega_{RF} \leq 0.5$ is satisfied, low offset frequencies can be used.

3.5.3 Effect of the crusher gradients

The percentage of the excited spins at different frequencies is related to the band of the RF pulse in the Fourier domain. For example, when a hard pulse with $8ms$ pulse duration and $4kHz$ offset frequency is used as an excitation pulse, simulations indicate that it causes excitation of 11% of the spins on the on-resonance, whereas for Fermi and SLR pulse shapes with the same pulse duration and offset frequency, excitation of the on-resonance spins is negligible. When the offset frequency of the pulse decreases, band of the pulse in the Fourier domain comes closer to zero frequency and as a result of that the spins on the on-resonance may excite. A similar scenario can be observed when the pulse duration decreases, since band of the pulse in Fourier domain increases.

In order to minimize the effect of the tilting the magnetization outside of the desired frequency, a sequence is modified by adding crusher gradients with $1ms$ duration. In order to observe the effect of these gradients another sequence is generated by removing crusher gradients and by applying the phase encoding gradient before the off resonant RF pulse and the phase results obtained with these sequences are compared. For these experiments $8ms$ hard, Fermi and SLR pulses with $4kHz$ and $1kHz$ offset frequencies are used. In Figure 3.7, comparison of the central line phase distributions obtained from phase images for each pulse shape and offset frequency is shown. For both $4kHz$ and $1kHz$ offset frequencies, when crusher gradients are applied to the sequence, the phase distribution for each pulse shape shows similar characteristics. However, when there is no crusher gradient, the effect of the tilting the magnetization outside of the region of interest can be seen on the phase distributions, especially on the results for hard pulse shape.

3.6 Discussion and Conclusion

In this study, we have presented a new approximated Fourier domain expression to increase the understandability of the BS based B_1 mapping method. Using this expression, $|B_1^+|$ values can be predicted from the phase data by using the Fourier transform of the BS RF pulse.

Simulations and experiments show that the method works well even for short pulse durations and low offset frequencies when the condition $\omega_1/\omega_{RF} \leq 0.5$ is valid. Note that the usage of a BS pulse with a short pulse duration is crucial to decrease the TE value and increase the magnitude signal and a low offset frequency can be preferable to increase the phase shift obtained by the method, especially for low B_1 magnitudes.

During these simulations and experiments crusher gradients were also used, as suggested in [41], and their effects were monitored. Our observations indicate that crusher gradients have to be used to remove the echo originating from tilting off-slice spins by the off-resonant pulse, especially when low offset frequencies and small pulse durations are used.

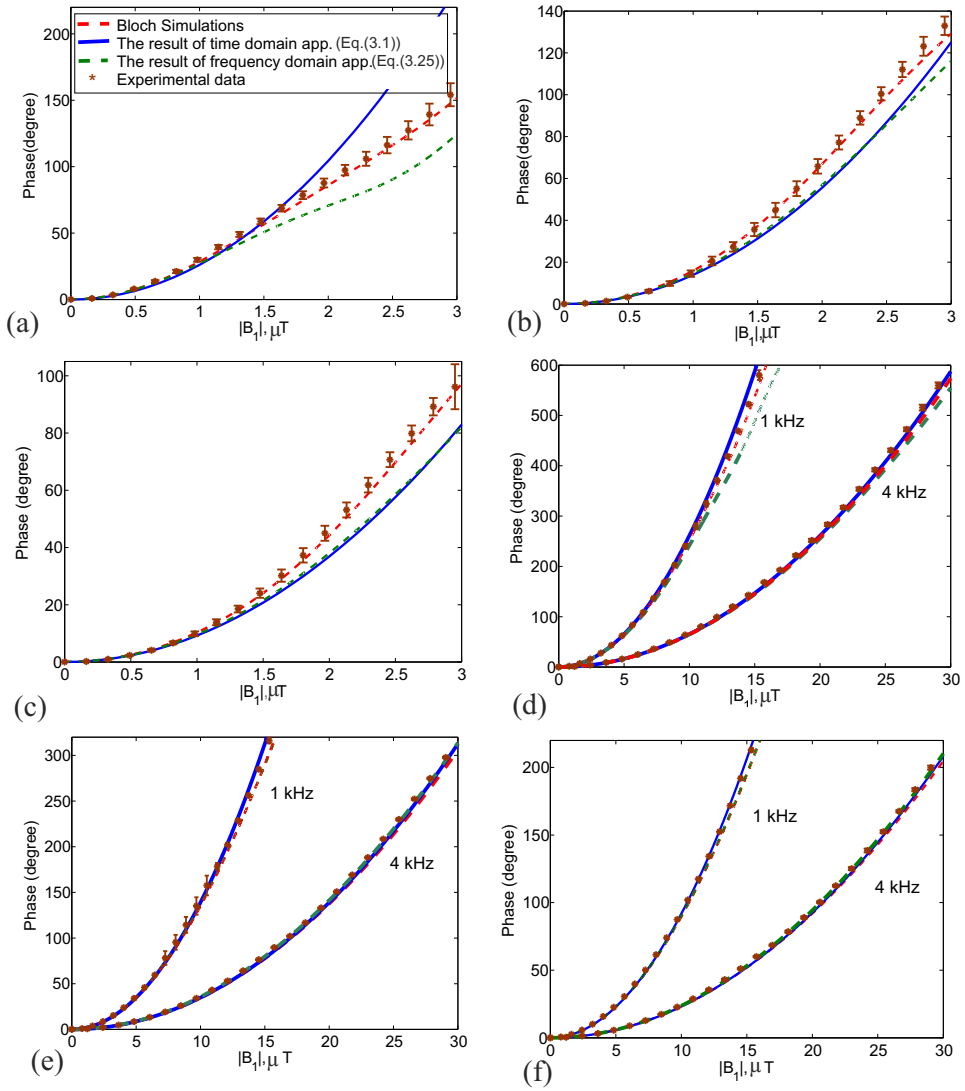

Figure 3.5: Relation of phase to magnitude of B_1 for (a) Hard, (b) Fermi, and (c) SLR pulses with 100 Hz offset frequency and 8 ms pulse duration. Relation of phase to magnitude of B_1 for (d) Hard, (e) Fermi, (f) SLR pulses with 1 kHz and 4 kHz offset frequencies and 8 ms pulse duration.

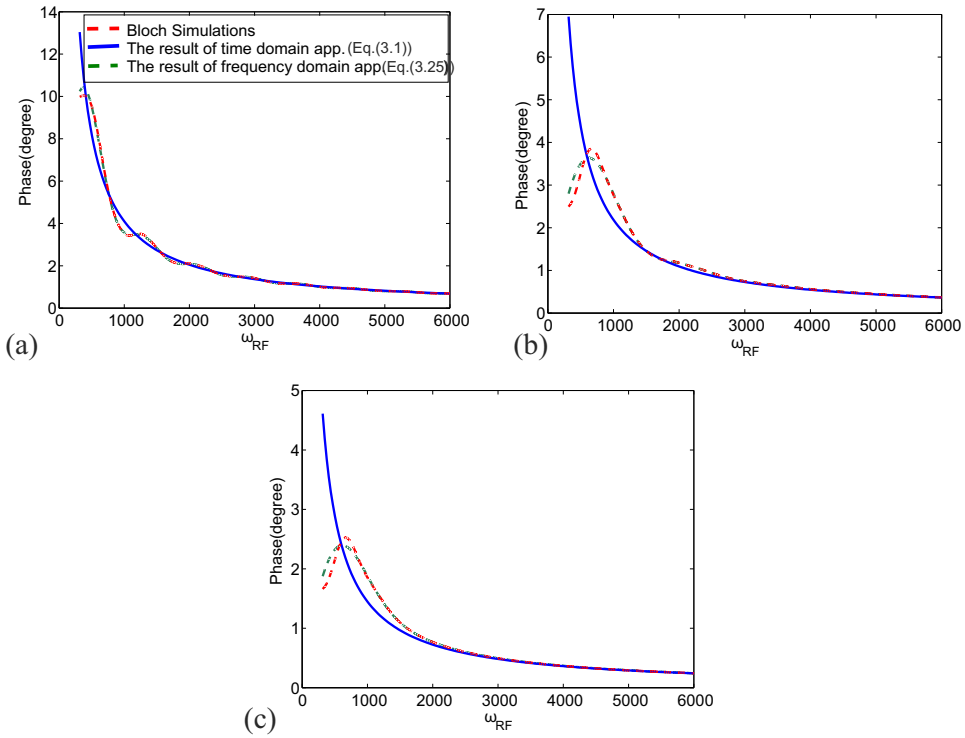

Figure 3.6: Relation of ω_{RF} to the phase shift for (a) Hard, (b) Fermi, and (c) SLR pulses with a 8 ms pulse duration and $|B_1^+| = 0.5\ \mu T$ (to satisfy the approximation $\omega_{RF} >> \omega_1$ where $\omega_1 = \gamma B_1$).

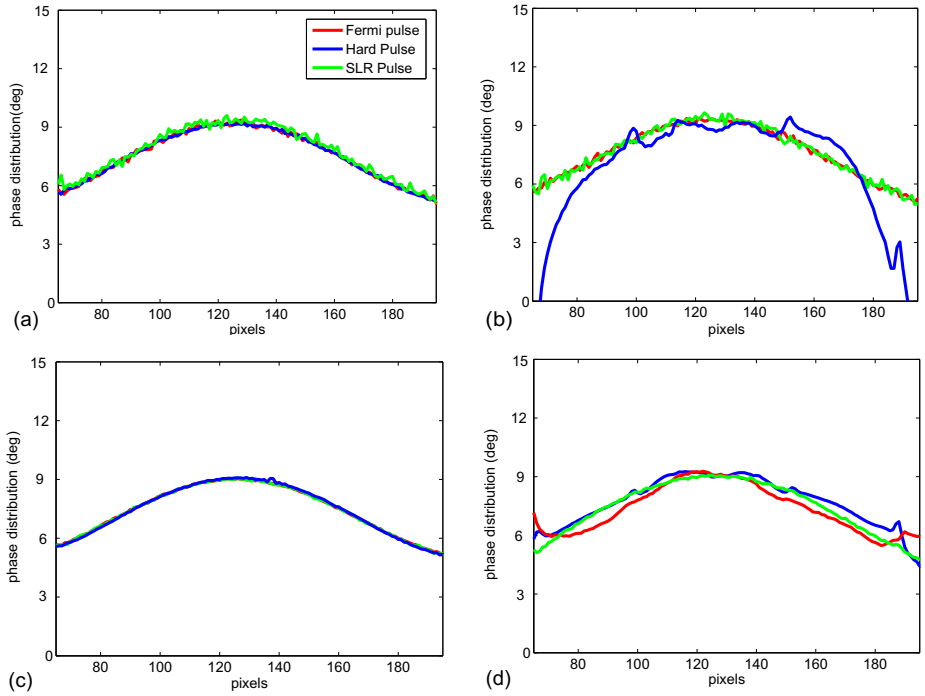

Figure 3.7: One line phase distribution patterns for (a) 8 ms Hard, Fermi and SLR pulses with 4 kHz offset frequency when there are crusher gradients (b) 8 ms Hard, Fermi and SLR pulses with 4 kHz offset frequency when there are no crusher gradients (c) 8 ms Hard, Fermi and SLR pulses with 1 kHz offset frequency when there are crusher gradients (d) 8 ms Hard, Fermi and SLR pulses with 1 kHz offset frequency when there are no crusher gradients.

Chapter 4

Imaging using B_1 gradients

4.1 Preface

The content of this chapter was presented in part at the Scientic Meeting of International Society of Magnetic Resonance in Medicine in 2013 [44].

4.2 Introduction

Current clinical MR systems use the main field gradient (B_0 gradients) for spatial MR signal encoding. Another solution to encode the spatial signal is to use the linear variations of the RF fields (B_1 gradients). MRI without B_0 gradients could alleviate several related disadvantages, including acoustic noise, eddy current problems, limited rise and fall times of gradient pulses, and peripheral nerve stimulation. Furthermore, when B_1 gradients are used instead of slice selection, phase encoding, and readout B_0 gradients, a gradient coil with expensive amplifiers can be removed from the MR system, giving the patient more space in the magnet bore and reducing the system cost.

On the other hand, B_1 gradients present some disadvantages. They have

smaller strength compared with B_0 gradients. Also, while using different RF coils to generate B_1 gradients in the three spatial directions a coupling problem can be observed, which may lead to artifacts in the image [45]. In earlier studies [45–47], usage of B_1 gradients instead of B_0 gradients has been proposed to encode the spatial information. In [46], it was demonstrated that B_1 gradients can be used in the detection of motion. [45] is a review article that surveys the capabilities of B_1 gradients in the domains already covered by B_0 gradients and evaluate their advantages and disadvantages with respect to B_0 gradients. In [47], a ladder-shaped coil was proposed to generate a constant B_1 gradient and images of water phantoms were obtained with the proposed coil.

In this study, we use B_1 gradients to encode flow along one direction and for shear wave imaging. For each case, the used methods and the performed experiments are discussed in the following sections in more detail.

4.3 Flow Imaging using B_1 gradients

4.3.1 Introduction

Magnetic resonance imaging is a non-invasive method to visualize the anatomy of the heart and vessels. In addition, the dynamic components of blood flow and cardiovascular function can be characterized with this imaging tool and this characterization provides insight into normal and pathological physiology.

Phase contrast (PC) MRI is a widely used method to visualize and quantify the blood flow and tissue motion by applying flow-encoding gradients [18–21]. In PC acquisitions, the velocity of the magnetization can be obtained from the phase of the image with the help of the flow-encoding gradients. The most common flow encoding gradient is a bipolar gradient, which comprises two lobes of equal area and opposite polarity. Because the net area under the bipolar gradient is zero, there is no net phase accumulation for stationary spins. On the other hand, for spins moving along the direction of the gradient, a net phase, which is linearly

proportional to the spins' velocity, accumulates [22]. In addition, the direction of the motion can be determined using the knowledge of the bipolar gradient axis.

In the literature, using B_1 gradients to encode flow was proposed as an alternative to conventional methodologies using B_0 gradients [48, 49]. The study in [48], combines gradient-recalled acquisition in a steady state with B_1 gradients. This approach is sensitive to the rate of blood flow and it is claimed that this method might be useful for imaging very slow, nonuniform flow through capillary beds and in the extravascular space. In [49], a new pulse sequence using B_1 gradients was proposed to determine the flow velocity. With this proposed sequence, the signal from the stationary samples was expected to be null.

In our study, we propose another solution to encode flow by using Bloch-Siegert (BS) [34, 42] phase shifts generated by a spatially dependent B_1 field. (Note that a similar idea was recently presented in [50] such that the properties of spatially dependent BS phase shift is used for phase encoding.) For two different pulse sequences using BS pulses, the solution is tested and the results of the experiments demonstrate the feasibility of using BS shift with B_1 gradients in detecting the flow.

4.3.2 Theory

In general, the phase of an MR signal can be expressed as:

$$\phi(\tau) = \gamma \int_0^\tau \bar{G}(t) \cdot \bar{r}(t) \mathrm{d}t \tag{4.1}$$

where $\bar{G}(t)$ is a time dependent B_0 gradient, $\bar{r}(t)$ is the position vector and γ is the gyromagnetic ratio. Basically, for a spin with a constant velocity, υ, and initial position, x_0, and for a bipolar gradient in the direction parallel to the flow with duration T and constant magnitude G, this phase becomes as follows:

$$\phi(\tau) = \gamma(\int_0^{T/2} G(x_0 + \upsilon t)\mathrm{d}t - \int_{T/2}^{T} G(x_0 + \upsilon t)\mathrm{d}t) \quad (4.2)$$

$$= -\gamma G \upsilon T^2/4. \quad (4.3)$$

As discussed in Section 3, the phase shift due to the Bloch Siegert shift can be written as follows:

$$\phi_{BS} \approx \int_{-T/2}^{T/2} \frac{\gamma^2 |B_1(t)|^2}{2\omega_{RF}(t)} \mathrm{d}t. \quad (4.4)$$

where ω_{RF} is the angular offset frequency of the Bloch Siegert pulse. When the offset frequency is changed from $+\omega_{RF}$ to $-\omega_{RF}$ at the half duration of the BS pulse, BS pulse acts like a bipolar pulse and in the case of inhomogeneous B_1 field, the flow data can be carried on the Bloch Siegert phase shift. Spatially variant B_1 field can be expressed as $B_1(t) = B_{10} + \nabla B_1 x(t)$, where B_{10} and ∇B_1 are the constant and the gradient parts of $B_1(t)$ field, respectively. When the spatially variant B_1 field has a bipolar behavior and $x(t) = \upsilon t$, the BS phase shift becomes:

$$\phi_{BS} \approx \int_{-T/2}^{0} \frac{\gamma^2 |B_{10} + \nabla B_1 x(t)|^2}{2\omega_{RF}(t)} \mathrm{d}t - \int_0^{T/2} \frac{\gamma^2 |B_{10} + \nabla B_1 x(t)|^2}{2\omega_{RF}(t)} \mathrm{d}t \quad (4.5)$$

$$\approx \frac{\gamma^2 B_{10} \nabla B_1 \upsilon T^2}{4\omega_{RF}(t)}. \quad (4.6)$$

Note that BS pulse shape is taken as a hard pulse shape. As shown in this approximate expression, the BS phase shift is proportional with the flow velocity. With the knowledge of the B_1 field distribution and the phase shift, the flow velocity can be estimated with this method. The usage and the verification of the proposed method are given in the following sections.

4.3.3 Materials and Methods

To verify the proposed method, two pulse sequences shown in Figure 4.1 are used. Both sequences are designed by modifying the sequence used in BS Shift B_1 mapping method. For sequence programming Siemens IDEA tool was used. In both sequences there are crusher gradients in the readout direction before and after the BS pulses to minimize the effect of the tilting the magnetization outside of the desired frequency (previously mentioned in Chapter 3). In the first sequence, there are two BS pulses separately with ω_{RF} and $-\omega_{RF}$ offset frequencies, whereas the initial RF pulse is at larmor frequency. In the second sequence two BS pulses are combined and the offset frequency is set as ω_{RF} for the first half duration and $-\omega_{RF}$ for the second half duration.

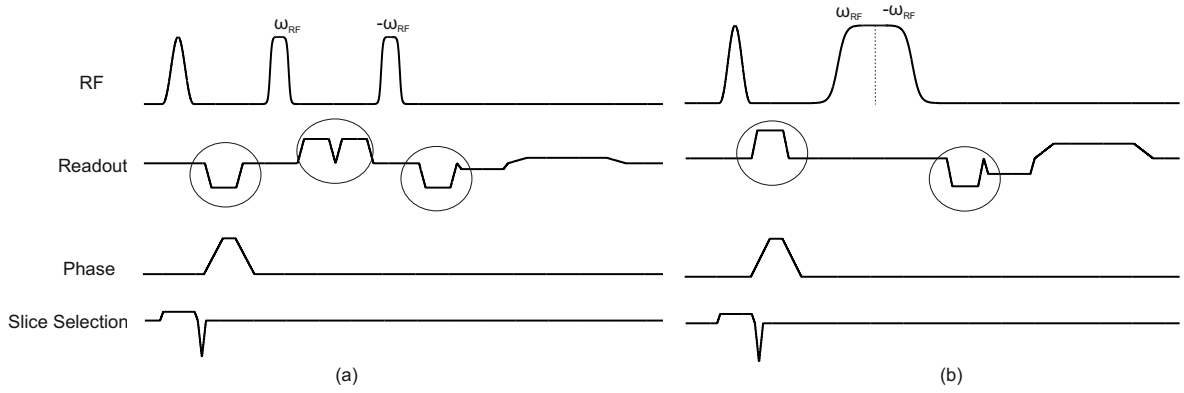

Figure 4.1: MR flow imaging pulse sequences using B_1 gradients and Bloch Siegert shift. Note that crusher gradients are indicated by the circles.

To check the reliability of the obtained flow velocity results with the proposed method, we also perform experiments using classical flow imaging method with bipolar B_0 gradients. The duration of the gradient and the maximum peak are set to 2.5 ms and 5mT/m, respectively. To remove the background phase from the desired phase shift, two images are acquired. The first image is acquired by using a BS pulse with the offset frequency of ω_{RF} for the first half and $-\omega_{RF}$ for the second half, whereas, the second image is acquired by using a BS pulse with the offset frequency of $-\omega_{RF}$ for the first half and ω_{RF} for the second half. For the experiments using B_0 gradients, again the difference of two acquisitions, one

with positive polarity flow encoding gradient and one with negative polarity is used.

All experiments were performed using a Siemens Magnetom TimTrio 3T scanner and transmit array system. To generate a uniform excitation, a birdcage coil is used and the BS pulses are transmitted with a 3 cm diameter loop coil. The experimental set-up is shown in Figure 4.2. Loop coil is placed perpendicular to B_0 field and its position inside the birdcage coil is arranged such that minimum coupling between the coils occurs. Direction of the flow is set to be in the x-axis. The B_1 maps of the coil to determine the B_1 gradient are obtained using BS Shift B_1 mapping method discussed in Chapter 3.

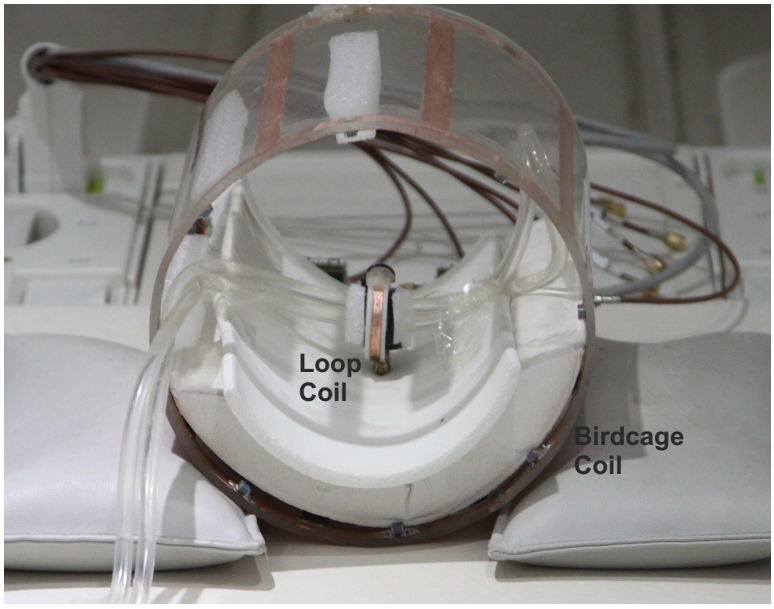

Figure 4.2: Flow imaging setup.

4.3.4 Experiments and Results

Figure 4.3 shows the B_1 and B_1 gradient maps of the loop coil for two water tubes. In these results FOV is 200mm and matrix=256x256. B_1 map and B_1 gradient map are normalized to the applied voltage. For the applied voltage during the experiments, the peak B_1 magnitude at the center ($x = 0$) is measured as $12.5\mu T$ and B_1 gradient for the slice at $x = 1cm$ is calculated as $2mT/m$, approximately.

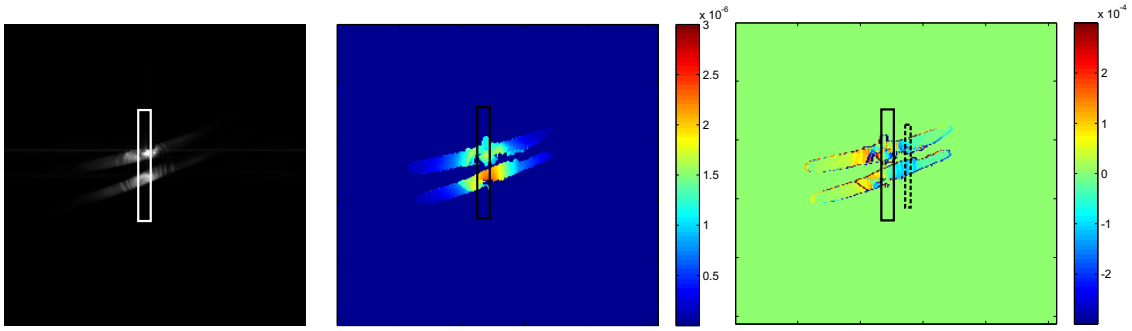

Figure 4.3: Images of two tubes in flow experiments (a) Magnitude image (b) B_1 map of the loop coil in terms of T/V (c) B_1 gradient map of the loop coil in terms of $Tm^{-1}V^{-1}$. (Note that rectangular shapes in each figure show the position of the coil and in (c) the rectangular shape with dash lines indicates the slice position for the experiments.)

Figure 4.4 demonstrates the magnitude and phase shift images of two tubes while water is flowing through the tubes in opposite directions. Imaging plane is chosen as perpendicular to the flow direction as shown with a dotted rectangular shape in Figure 4.3-(c). It is placed on yz-plane at 1cm distant from the loop coil. The imaging parameters were: FOV=80mm, TR/TE=100ms/14.5ms, matrix=256x256 and slice thickness=5mm. The phase difference image obtained by using bipolar flow encoding B_0 gradients is shown in Figure 4.4-(b). When the first sequence given in Figure 4.1 is used, the phase shift is obtained as given in Figure 4.4-(c) and similarly, when the second sequence given in Figure 4.1 is used, the phase shift is obtained as given in Figure 4.4-(d).

As shown in Figure 4.4-(b), the phase difference encoded by bipolar flow encoding B_0 gradients is around $\pm 0.78\ rad$. Using Eq. 4.3 and the specified parameters for the bipolar gradient (2.5ms duration and 5mT/m gradient magnitude), the flow velocity along the x-axis is calculated $\pm\, 0.36 m/s$ for $\pm 0.78\ rad$ phase difference. In Figure 4.4-(c) the phase difference image encoded with the first proposed sequence, in which two separate BS pulses are used, is demonstrated. This experiment was repeated 3 times and the mean flow velocity along the x-axis is calculated as $\pm(0.35 \pm 0.07) m/s$ with the help of Eq. 4.6. Similarly, Figure 4.4-(d) shows the phase difference image encoded with the second proposed method

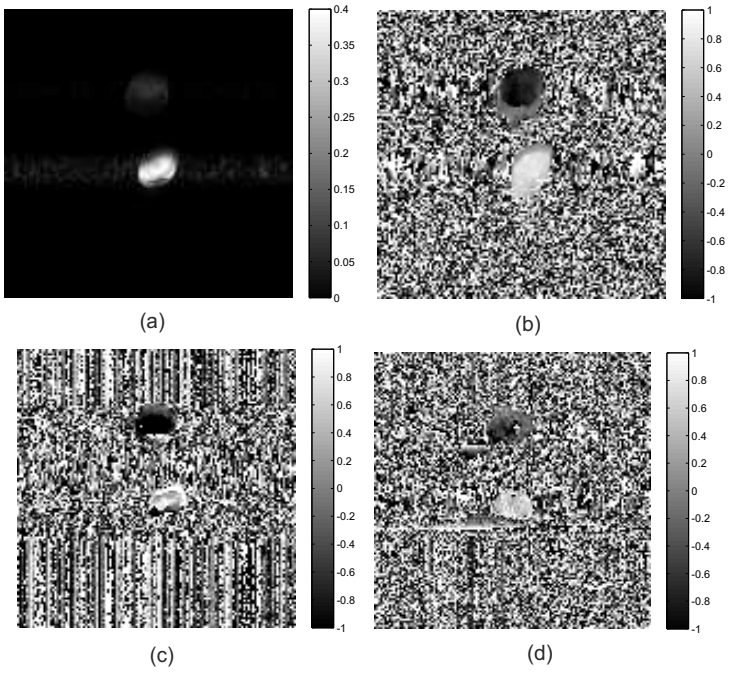

Figure 4.4: Images of two tubes with a water flow in opposite directions(a) Magnitude image. Phase difference image obtained with (b) Bipolar flow encoding B_0 gradients, (c) First proposed sequence, (d) Second proposed sequence.

using BS shift. Again, the experiment was repeated for 3 times and the mean flow velocity along the x-axis is calculated as $\pm(0.29 \pm 0.025)m/s$.

Flow imaging experiments were repeated for the case that an imaging plane was chosen parallel to the flow direction. Figure 4.5 shows the B_1 and B_1 gradient maps normalized to the applied voltage used in the experiments. For these experiments, FOV was set as 80mm and matrix was 128×128. Figure 4.6 demonstrates the magnitude and phase difference images obtained with the proposed flow encoding methods. In Figure 4.6-(c) and (d), the flow seems to change direction along a single tube, since the direction of the B_1 gradient changes at two sides of the coil. So, both the magnitude and the direction of the B_1 gradient have to be taken into account to calculate the flow velocity. Figure 4.7 shows the flow velocity maps obtained by three different methods. The difference between the calculated flow velocities obtained by bipolar flow encoding B_0 gradients and BS shift based flow encoding method is less than 10%. For the second proposed method which uses a BS pulse with the offset frequency of ω_{RF} for the first half

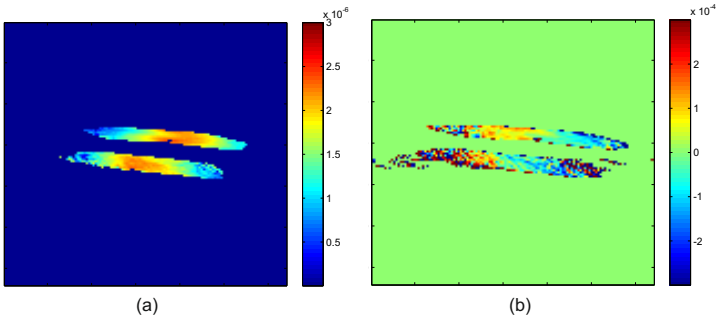

Figure 4.5: (a) B_1 map of the loop coil (in terms of T/V) (b) B_1 gradient map of the loop coil in terms of T/m/V.

and $-\omega_{RF}$ for the second half, the distortion in the phase difference image also disturbs the flow velocity map. The possible reason for this distortion is the nonuniform offset frequency change in a BS pulse.

The results of the flow calculations indicates that when a sufficient B_1 gradient is generated at the volume of interest, BS shift pulses can be used for flow imaging similar to the bipolar B_0 gradients.

4.3.5 Conclusion

The main aim of this study is to demonstrate the feasibility of using B_1 gradients instead of B_0 gradient. In this study, we have proposed two sequences using Bloch Siegert shift and B_1 gradients to encode the velocity of the flow. This is an alternative solution to the flow imaging using bipolar B_0 gradients. The proposed method has been experimentally verified by comparing the resultant velocity measurements obtained by using bipolar flow encoding B_0 gradients. As mentioned before in [49], using B_1 gradients makes it possible to encode very slow motions. As a result, our proposed sequences can also be used as alternative solutions to encode slow motions.

On the other hand, the proposed flow encoding methods suffer from the problems observed in the BS shift based methods. Since the BS pulses may cause undesired magnetization tilting, high crusher gradients are needed to suppress

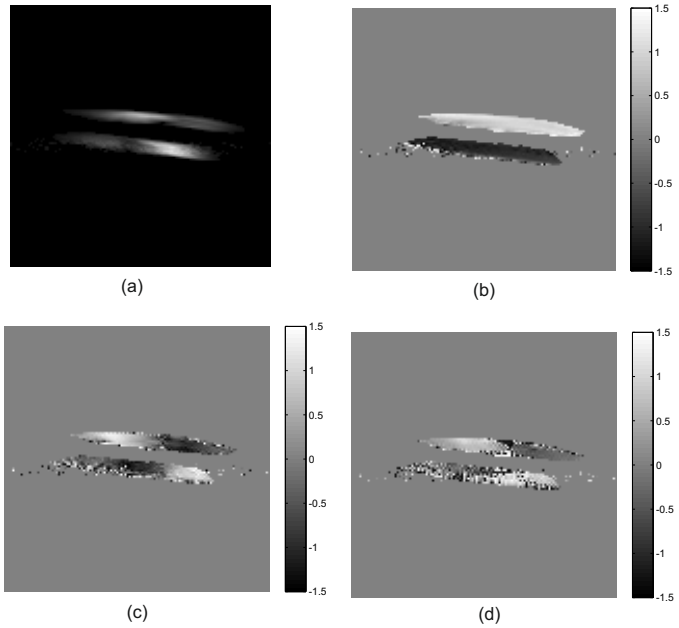

Figure 4.6: Images of two tubes with a water flow in opposite directions(a) Magnitude image. Phase difference image obtained with (b) Bipolar flow encoding B_0 gradients, (c) First proposed sequence, (d) Second proposed sequence.

this effect. If the crusher gradients are insufficient, the undesired off-slice spins may cause distortion in the resultant image and that may also affect the flow velocity map. Besides, nonlinear B_1 gradients in the other directions (i.e. different than the flow direction) have to be taken into account for reconstruction of the flow maps. Note that the reconstruction algorithms of a flow map is not investigated in this study.

4.4 Shear Wave Imaging using B_1 gradients

4.4.1 Introduction

Manual palpation is the standard technique used to understand stiffness change in tissues (especially in the breast tissue) and to detect symptoms of diseases. However, this method is not useful in the detection of the tumor and its size

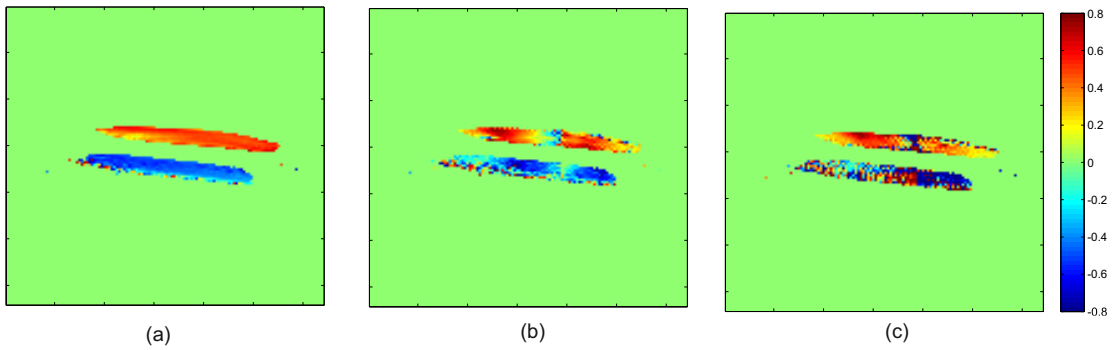

Figure 4.7: Flow velocity maps (in terms of m/s) obtained with (a) Bipolar flow encoding B_0 gradients, (b) First proposed sequence, (c) Second proposed sequence.

when the tumor is inaccessible [51]. Magnetic resonance elastography (MRE) is a non-invasive imaging technique used for the visualization of elastic properties of biological tissues. By this technique, the propagation of the low frequency transverse acoustic strain waves in tissue-like media can be directly visualized [23]. MRE is a phase contrast based method similar to the methods used in flow and diffusion imaging in MRI [22]. The technique proposed in [23] is a fully dynamic phase contrast method in which a cyclic motion generated in the tissue is synchronized with the motion sensitization gradients. Resultant MR phase images carry information regarding particle displacements due to this motion. By analyzing these images, the transmission of shear waves in a tissue can be captured.

Currently, MRE is being used clinically in breast and liver tissues as a diagnostic tool and the experimental studies are being continued in brain, cardiac, hyaline cartilage, bone, lungs, blood vessels and prostate [52–56]. In these studies, to increase the spatial resolution, the frequency of the applied shear waves is increased. But, high frequency waves attenuate much faster than low-frequency waves. As a result, design of a suitable actuation system becomes important. Similarly, for very stiff tissues such as bone and cartilage, much higher vibration frequencies (in the kilohertz range) than soft tissues are required to evaluate the elasticity. Especially for the early diagnosis of the osteoarthritis, and degenerative disc disease that causes low back pain, non-invasively measuring cartilage and

bone elastic properties becomes critical [55, 57]. However, current clinical MRI scanners cannot encode wave motion at such high frequencies due to the gradient hardware limitations. As a solution for this problem, in [24], a specific actuator and gradient hardware was constructed. But using gradient coils at higher frequencies causes an increase in the eddy currents induced by fast switching rates. Furthermore, using gradient coils at higher frequencies can cause an increase in the noise and it may also increase the risk of peripheral nerve stimulation.

In our study, we propose to use B_1 gradients instead of B_0 gradient as an alternative solution to the solution presented in [24]. In our solution, the signal is received only from the spins with motion at the desired frequency and therefore the displacement of the shear wave can be calculated by using the magnitude image. To verify the method, phantom experiments are performed and it is shown that B_1 gradients can be used to detect the shear properties of investigated tissues at frequencies in the kilohertz range.

4.4.2 Theory

The phase of the transverse plane magnetization can be written as follows:

$$\phi(\tau) = \gamma \int_0^\tau \bar{G}(t) \cdot \bar{r}(t) \mathrm{d}t \tag{4.7}$$

where $\bar{G}(t)$ is time dependent B_0 gradient, $\bar{r}(t)$ is the position vector and γ is the gyromagnetic ratio. For the case of propagating shear wave, position vector $(\bar{r}(t))$ can be expressed as the following:

$$\bar{r}(t) = \bar{r_0} + \bar{\xi_0} exp(-j(\bar{k} \cdot \bar{r} - \omega t + \alpha)) \tag{4.8}$$

where $\bar{r_0}$ is the mean position, $\bar{\xi_0}$ is the peak displacement, ω is the angular frequency of the mechanical excitation or the modulation frequency of the focused ultrasound to generate the shear wave, $\bar{k}$ is the wave number and α is the initial phase offset between the wave generation and the motion encoding gradients. For

a trapezoidal gradient shape with magnitude G and the negligible ramp times, the phase relation becomes [23]:

$$\phi(\tau) = \frac{2\gamma NT(\bar{G} \cdot \bar{\xi_0})}{\pi} sin(\bar{k} \cdot \bar{r} + \alpha) \tag{4.9}$$

where T is the period of the motion encoding gradient cycles and N is the total number of these cycles. If the motion encoding gradients are sinusoidal, the phase relation becomes [23]:

$$\phi(\tau) = \frac{\gamma NT(\bar{G} \cdot \bar{\xi_0})}{2} cos(\bar{k} \cdot \bar{r} + \alpha) \tag{4.10}$$

For a typical clinical MR scanner, the maximum gradient amplitude and slew rate limitations are given as 22 mT/m and 120 mT/m/msec, respectively [24]. To encode the shear waves propagation accurately the phase shift has to be high. Because the phase shift is proportional with the gradient magnitude, strong magnetic gradients are needed for high phase shifts. However, when the frequency of the shear wave is higher than 2 kHz, the maximum gradient magnitude that can be generated falls below 10 mT/m due to the hardware limitations. This inverse relation between the gradient magnitude and the frequency causes a decrease at the phase shift for high vibration frequencies. On the contrary, when B_1 gradients are used instead of B_0 gradients, the frequency of the B_1 field can be increased while the peak B_1 gradient magnitude is being kept same.

In this study, we propose to use RF gradients to encode shear wave at frequencies in kilohertz range which is a similar approach proposed in [49] to measure the slow coherent motion. In our method, the phase of the RF pulse is alternated from 0 to π in synchrony with motion and the expected signal for the proposed method is as follows:

$$M_{xy} = M_0 sin(\gamma \int_0^{\tau} B_1(r(t), t) \mathrm{d}t) \tag{4.11}$$

where M_{xy} is the transverse component of the magnetization, M_0 is the initial

magnetization, $B_1(r(t),t)$ is the inhomogeneous RF field and τ is the pulse duration. When $B_1(r(t),t)$ is defined as $B_1(r(t),t) = B_1 + \nabla B_1 r(t)$, where ∇B_1 is the B_1 gradient, B_1 is the constant RF field, and $\bar{r}(t) = \bar{r_0} + \bar{\xi_0} exp(-j(\bar{k}\cdot\bar{r} - \omega t + \alpha))$, the final expression becomes:

$$M_{xy} = M_0 sin\Big(\frac{2\gamma\tau(\nabla\bar{B}_1 \cdot \bar{\xi_0})}{\pi} sin(\bar{k}\cdot\bar{r} + \alpha)\Big) \tag{4.12}$$

In this expression, the resultant signal becomes zero when there is no motion which means that the expected signal comes only from the spins with motion at the same frequency with the frequency of the generated wave. This expression also shows that the flip angle of the signal is directly proportional with the displacement of the tissue when RF field has a constant gradient.

In the following sections, the usage of the typical MR elastography method, the usage and the verification of the proposed method in this study are given.

4.4.3 Materials and Methods

Typical MRE sequence using sinusoidal motion encoding gradients is given in Figure 4.8. In order to remove the background phase form the desired phase shift, two images are acquired, one with positive polarity motion encoding gradient and one with negative polarity. The phase difference of these two acquisitions produce twice the phase shift given in Eq. 4.10 [58].

Initially, MR elastography method using the sequence given in Figure 4.8 is tested with phantom experiments. In these experiments two actuator systems, electromagnetic actuator and high-powered focused ultrasound (FUS), are used to generate shear waves in the desired region.

Figure 4.9 shows MR elastography setup using electromagnetic actuator. The z-axis is the parallel axis to B_0 field and the normal vector to the plane of the actuator coil is oriented perpendicularly to B_0 field. The coil is connected to the excitation plane which is positioned on the object under investigation. Applying

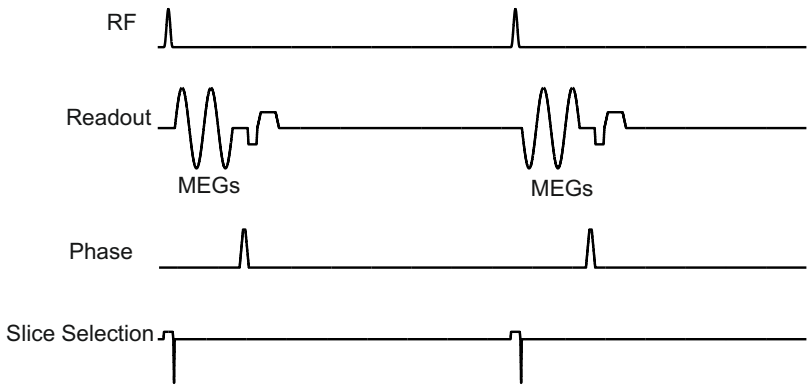

Figure 4.8: MR elastography pulse sequence diagram using motion encoding gradients (MEGs). Note that in this plot MEGs are on readout direction and its place can be changed according to the direction of the motion.

an alternating current results in periodic oscillation of the coil and this periodic motion is transferred to the excitation plate [59, 60]. The shear wave excitation with this actuator becomes only parallel to axis of B_0 field, z-axis.

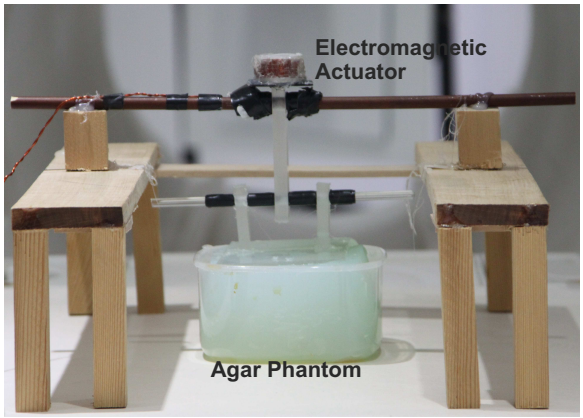

Figure 4.9: MR elastography setup using electromagnetic actuator, direction of the motion is along the z-axis.

Note that, electromagnetic drivers are inexpensive and simple in terms of design and implementation. Amplitude of the vibration depends on the number of the turns, current induced in the coil and the diameter of the coil. The main problem related with this actuator system is that, due to the current in the coil, imaging

artifacts may occur.

High-powered focused ultrasound transducer used in the experiments is a single element power transducer designed by IMASONIC. The transducer has a diameter of 50 mm, a focal length of 50 mm, and was operated at a frequency of 1MHz. The efficiency from electrical power to acoustical power is given as 80%. The experimental set-up is shown in Figure 4.10. FUS transducer is placed inside a water tank and a phantom is on a latex layer above the transducer. For the experiments, the peak of the motion encoding gradient is set to 20mT/m and the multiplication of the cycle number and the period (NT) is kept constant at 40ms. The imaging parameters were: FOV=200mm, TR/TE=100ms/44.5ms, matrix=256x256 and slice thickness=5mm.

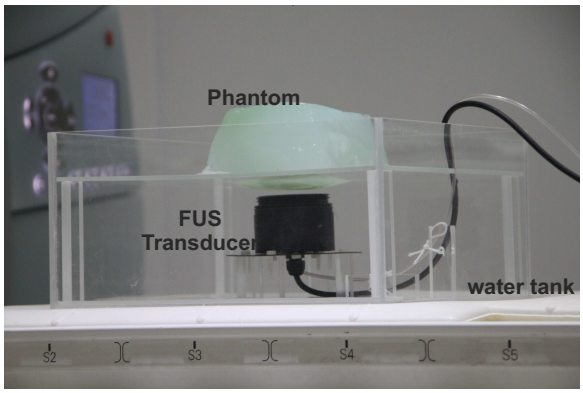

Figure 4.10: MR elastography setup using electromagnetic actuator, direction of the motion is along the z-axis.

During FUS experiments, to monitor the temperature increase at the focal region, temperature maps are also obtained. It is known that the water proton resonance frequency (PRF) depends on the local magnetic field strength. When temperature increases, the magnetic field in the medium decreases and there is a linear relationship between PRF shift and temperature change given as follows [61]:

$$\Delta\phi_T = \alpha\gamma B_0 TE\Delta T, \tag{4.13}$$

where $\Delta\phi_T$ is the phase change, γ is the gyromagnetic ratio, α is the PRF-thermal coefficient, B_0 is the static magnetic field, TE is the echo time and ΔT is the

temperature change. In calculations α is taken as $-0.01 ppm/^{\circ}C$.

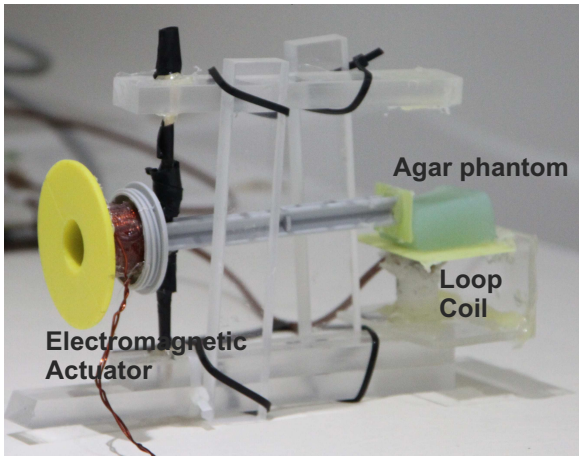

Figure 4.11: MR elastography setup using electromagnetic actuator for high vibration frequencies.

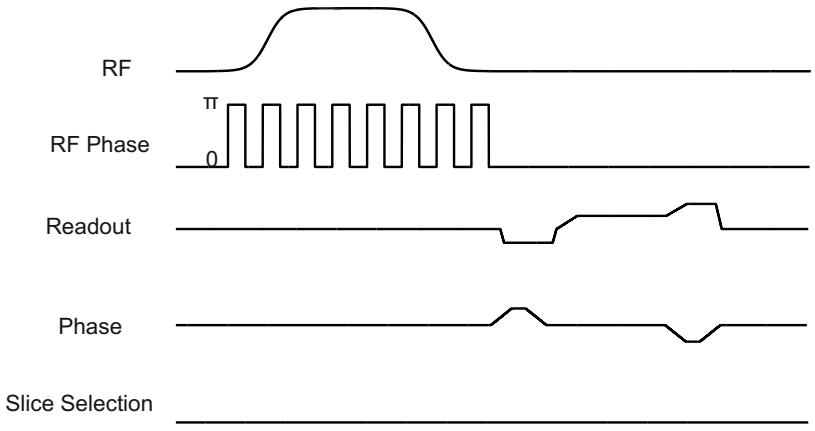

Figure 4.12: MR elastography pulse sequence diagram using B_1 gradients.

For the MRE experiments using B_0 gradients, the frequency range was kept between 100Hz to 1kHz. At shear wave frequencies above 1 kHz, the phase values decrease due to the decrease in B_0 gradients. At shear wave frequencies higher than 1kHz, we tested our new approach using B_1 gradients to detect the shear wave. In Figure 4.11, the experimental setup is shown. To generate sufficient vibration at the frequencies in kilohertz range, a new electromagnetic actuator was built similarly as proposed in [24]. The frequency range of the actuator,

in which a sufficient displacement in the tissue can be generated, is measured between 1kHz to 5kHz [62]. The direction of the generated shear wave is along z-axis. $\%4 - \%5$ agar phantoms with $2 \times 1 \times 3$cm dimensions are prepared to be used as a model of the stiff and small tissue (e.g. cartilage tissue). To acquire a sufficient B_1 gradient value that could be used in the detection of the shear wave displacement, a simple one turn loop coil with $1cm$ diameter was used. The loop coil is placed under an agar phantom perpendicular to the B_0 field. The B_1 maps of the coil are obtained using BS Shift B_1 mapping method, discussed in Chapter 3.

Figure 4.12 shows the pulse sequence used in this approach. A Fermi pulse shape is used as an envelope of the excitation pulse instead of a hard pulse and the phase of the pulse is alternated from 0 to π periodically with the period of the vibration. (Note that, a Fermi pulse can be defined as a rectangular pulse with ramps.) The imaging parameters were: no slice selection, FOV=116mm, TR=100ms and matrix=256×256. Note that, because the band of the excitation pulse is wide, no slice selection is used and phantom size is adjusted as a one slice thickness. On the other hand, slice selection can also be used, since a Fermi pulse has smaller band than the band of a hard pulse.

All experiments were performed using a Siemens Magnetom TimTrio 3T scanner. By using MR external trigger, the RF cycles and motion encoding gradients are synchronized with the mechanical wave.

4.4.4 Experimental Results

In Figure 4.13, propagation of a half cycle sinusoidal shear wave with 5ms duration (i.e. half cycle of a sinusoidal pulse with 100Hz frequency) is demonstrated with the phase images obtained for five different time delays between the motion encoding gradients and the motion. In this experiment, the imaging parameters are set as: FOV=200mm, matrix=256×256, and TR=100ms. Since starting time of motion encoding gradients is shifted as much as the time delay, images

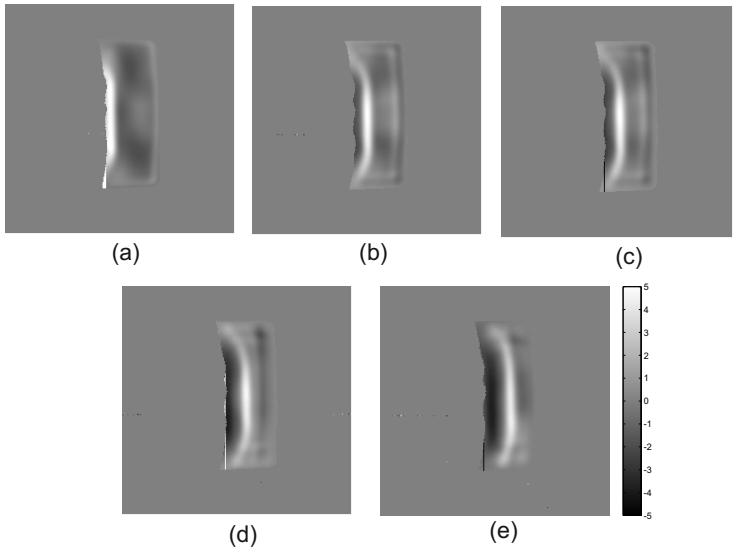

Figure 4.13: Phase images when the time delay between the motion encoding gradient and motion is (a) 0ms, (b) 8ms, (c) 10ms, (d) 15ms, (e) 20ms.

for TE=$\{10, 18, 20, 25, 30\}$ are observed. As mentioned before, an electromagnetic actuator is used to generate shear waves along the z-axis. The imaging plane is set as the transverse plane (xy-plane, perpendicular to the shear wave direction) and motion encoding gradients are applied along the slice selection direction, parallel to the motion direction. Because of rapid phase changes in the images (i.e. 2π phase jumps), phase unwrapping algorithm is applied to each phase shift image. Using the propagation of the wave, the wave velocity is calculated as $(1.06 \pm 0.1)m/s$ for 1% agar phantom.

Figure 4.14 demonstrates the shear wave propagation generated at the focal region in the phantoms while using FUS transducer with 100Hz and 200Hz modulation frequencies. Note that, for this figure, the principal axis of the ultrasound beam is perpendicular to the image plane. The motion encoding gradients were applied in the same direction with the motion, which was also perpendicular to the image plane. For each frequency, the phase shifts were obtained for zero and π phase delays between the motion encoding gradients and the motion. The electrical power to the transducer was 12.5W and no temperature increase was

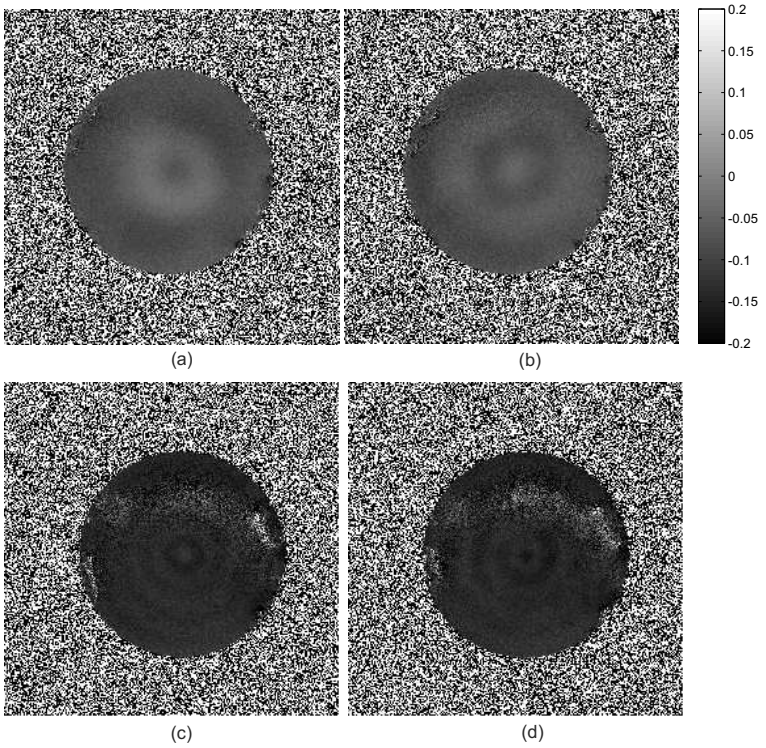

Figure 4.14: Phase difference images of coronal section of agar phantoms (a) 100Hz modulation frequency with zero phase delay, (b) 100Hz modulation frequency with π phase delay, (c) 200Hz modulation frequency with zero phase delay, (d) 200Hz modulation frequency with π phase delay.

observed at the focal region during these agar phantom experiments. Using the propagation of the wave, the wave velocity is calculated as $(2.9 \pm 0.3)m/s$ for a 2% agar phantom.

In order to analyze a temperature increase around the focal region and the acoustic path of the transducer, an experiment with bovine muscle was performed. In Figure 4.15, the magnitude image and the temperature map is given when the electrical power to the transducer was 24.5W. (Note that the FUS transducer is on with 1/10 duty cycle for 2.4min sequence duration.) At the end of 2.4min, the maximum temperature increase was around 8° at the focal region and there was not a notable temperature increase along the acoustic path of the transducer, as expected.

For the MRE experiments that the new method was tested, B_1 field gradients

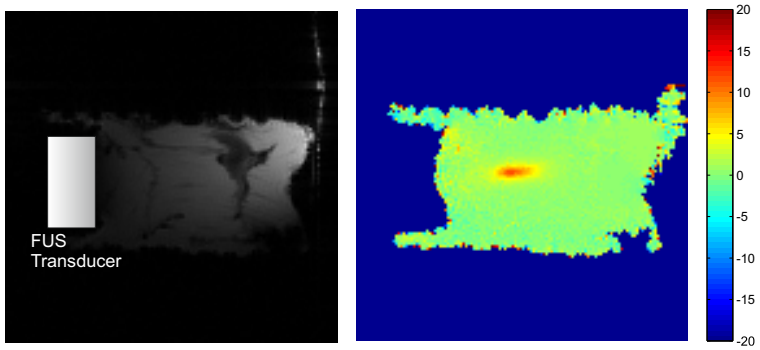

Figure 4.15: (a) Magnitude image of a bovine muscle, (b) Temperature change at the focal region and the acoustic path of the transducer.

of the loop coil is calculated from the B_1 maps. In Figure 4.16, B_1 map, B_1 contour plot and the B_1 gradient map are shown for the xz-plane, which is the perpendicular plane to the normal axis of the coil. Figure 4.16-(c) shows that at both edges of the phantom there is approximately 5mm region with constant B_1 gradient magnitude. Note that, because the phantom used in the experiments has a one slice thickness, we assumed that the field variation on the parallel plane to the normal axis of the coil is negligible. By using the linear relation between the applied voltage and the peak magnitude of the B_1 field, B_1 gradient magnitude is adjusted to $25mT/m$.

The proposed method using B_1 gradients was tested for three different vibration frequencies, 2kHz, 3kHz and 4kHz. Figure 4.17-(a),(b) and (c) demonstrate the magnitude images obtained with the method using B_1 gradients for 2kHz, 3kHz and 4kHz shear wave frequencies, respectively. Their one line plots (signal versus position plots) obtained along the white dashed lines are also shown in Figure 4.17(d),(e) and (f) for 2kHz, 3kHz and 4kHz vibration frequencies, respectively. The wavelength of the shear wave for each vibration frequency and the wave velocities are calculated approximately with the help of these one line plots. Each experiment was repeated 3 times for 5% agar phantom. For 2kHz shear wave frequency, the mean wave velocity is calculated as $(11.5 \pm 1.4)m/s$ by using the wavelength measurement. Similarly for 3kHz and 4kHz shear wave frequencies,

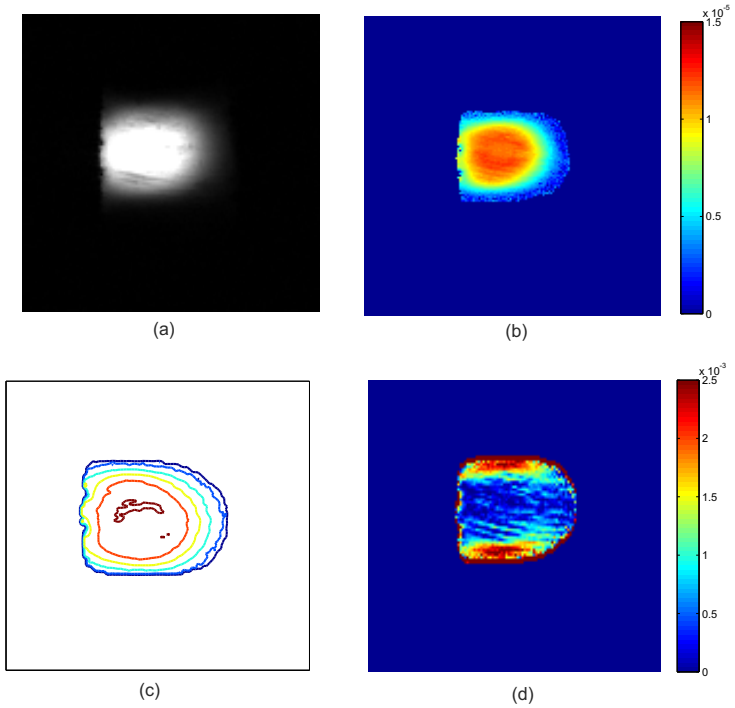

Figure 4.16: (a) B_1 map of 1 cm loop coil in xz-plane, (b) Contour plot for the B_1 map, (c) B_1 gradient map obtained from B_1 map.

the mean wave velocities are calculated as $(12.2\pm1.4)m/s$ and $(12.9\pm1.3)m/s$, respectively. On the other hand, if the initial magnetization, M_0 is known, the wave displacement in the tissue can also be calculated. Note that the reconstruction algorithms of a stiffness map is not investigated in this study.

4.4.5 Conclusion and Discussion

In this study, typical MR elastography method was tested with two different actuators, the electromagnetic actuator and FUS transducer. With the help of these initial studies, the problem due to the gradient hardware limitations was defined. As a result a method using B_1 gradients instead of B_0 gradients has been proposed. In this method, spins are excited by B_1 gradients and only the signal from the spins with motion is carried on the magnitude images.

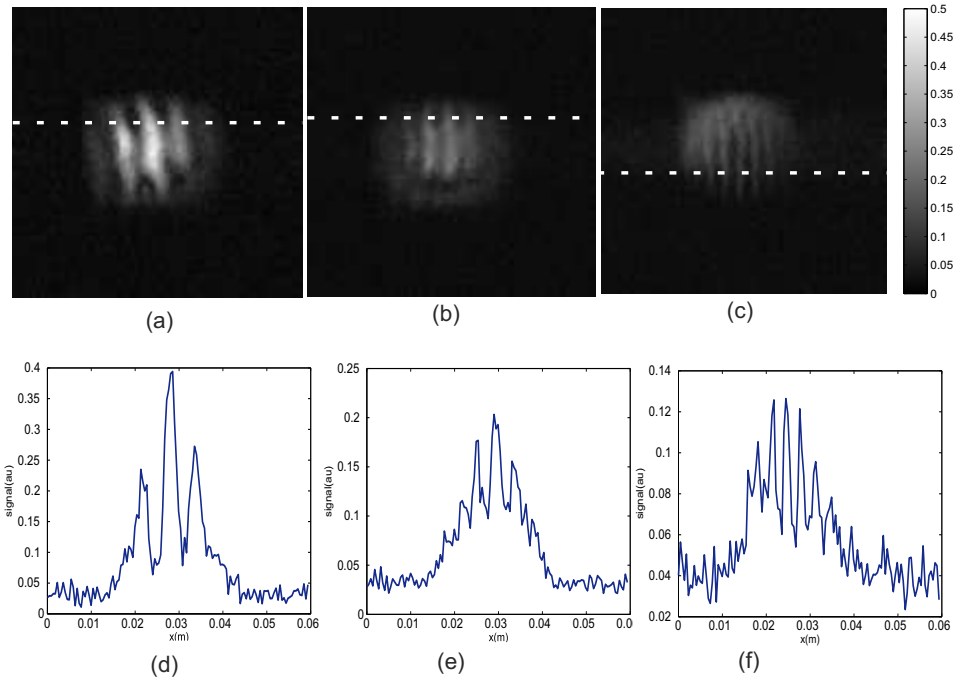

Figure 4.17: Magnitude images obtained with the method using B_1 gradients for (a) 2kHz, (b) 3kHz, (c) 4kHz vibration frequencies. One line plots (signal versus position plots) obtained along the white dashed lines on magnitude images for (d) 2kHz, (e) 3kHz, (f) 4kHz vibration frequencies.

The experiments are verified that B_1 gradients can be used to detect the shear properties at the frequencies in the kilohertz range instead of the B_0 gradients. With this alternative method the limitations due to finite rise- and fall-time of the gradient waveforms and therefore the maximum frequency of the wave that can be detected in the tissue can be solved. So, it would be possible to measure the mechanical properties of a very stiff and small tissues (e.g. cartilage) inside the body. Besides, TE value used in this method is much shorter than TE values used in the method based on motion encoding B_0 gradients. Note that, usage of short TE values is one of the major issues to prevent a signal loss. For instance, the used TE value in [55] is 24ms ,whereas with our method, this value is only 7ms which is an important improvement especially for imaging the tissues such as cartilage.

On the other hand, as a limitation in order to obtain the desired B_1 gradient at the level of B_0 gradient, very high RF power is needed and that may cause

an increase in the specific absorption rate(SAR). To solve this safety problem, longer TR durations can be used. Another disadvantage is related to the high sensitivity of the method to the inhomogeneity of the B_0 field. When there is an inhomogeneity in the B_0 field, the stationary spins may tilt and that causes an artifact. One of the solution for this problem can be to improve the shimming. Besides, nonuniform phase alternation of RF pulse due to hardware or programming errors also causes spins to tilt. To solve this problem, design of the RF pulse has to be optimized.

In this study the proposed method, using B_1 gradients for shear wave imaging, was tested only for a single motion direction. To improve the proposed method, the next step is to design an RF coil system to generate gradients in each directions. With the help of the TX-array system, RF coils, generating B_1 gradients in three directions, can be driven separately.

Chapter 5

Conclusion

In this dissertation, B_0 and B_1 gradients in MRI are analyzed and novel methods using B_1 gradients are proposed. In the first study of this thesis, safety of the gradient fields for the patients with active implantable medical devices is investigated. Specifically, simplified expressions for the electric field inside the cylindrical homogeneous body model for a perfectly uniform gradient field are derived to understand the nerve stimulation risk when there is an implant. Reliability of the expressions are tested with multiple phantom and ex-vivo experiments. In the second study, Bloch-Siegert shift B_1 mapping method are analyzed and a new approximated Fourier domain expression is proposed to increase the understandability of the method. Fourier domain expression increase the usability of the B_1 mapping method for short Bloch Siegert pulse durations and low offset frequencies. In the third study, B_1 gradients are studied with the purpose of imaging flow and shear waves. For flow imaging using B_1 gradients, the same idea in the Bloch-Siegert shift B_1 mapping method is used and the flow velocity is related to the Bloch-Siegert phase shift and B_1 gradient. On the other hand, in shear wave imaging using B_1 gradients, B_1 gradients are used in the initial excitation and the information of the displacement of the motion is carried on the magnitude signal. It is shown that maximum frequency limitation due to the finite rise- and fall-time of the gradient waveforms can be solved with B_1 gradients.

The practical applications of the studies presented in this thesis may be listed

as below. The first study presented in this thesis indicate that extensive analysis of B_0 gradients in MRI is important for safety issues. By using realistic simplifying assumptions, it is possible to obtain simplified electric field expressions that might help in formulating worst-case scenarios for stimulation risks of patients with implants, which might assist in performing MRI on these patients. The second study presented in this thesis can be used in devising a more accurate Bloch-Siegert shift based B_1 mapping method. The third study presented in this thesis can be used for B_1 gradient based imaging of flow and shear waves where usage of B_0 gradients are insufficient. As an example, imaging of slow flows as seen in capillaries or imaging of shear waves in stiff tissues such as cartilage can be performed using the methods proposed in this study.

Bibliography

[1] E. A. Turk, E. Kopanoglu, S. Guney, K. E. Bugdayci, Y. Z. Ider, V. B. Erturk, and E. Atalar, "A simple analytical expression for the gradient induced potential on active implants during MRI," *Biomedical Engineering, IEEE Transactions on*, vol. 59, no. 10, pp. 2845–2851, 2012.

[2] B. A. Chronik, "Peripheral nerve stimulation in MRI gradient coils," *Proceedings of the 16th Annual Meeting of ISMRM, Berlin, Germany*, 2007.

[3] F. Liu, H. Zhao, and S. Crozier, "On the induced electric field gradients in the human body for magnetic stimulation by gradient coils in MRI," *IEEE Trans. Biomed. Eng.*, vol. 50, no. 7, pp. 804–815, 2003.

[4] P. P. M. So, M. A. Stuchly, and J. A. Nyenhuis, "Peripheral nerve stimulation by gradient switching fields in magnetic resonance imaging," *IEEE Trans. Biomed. Eng.*, vol. 51, no. 11, pp. 1907–1914, 2004.

[5] J. A. D. Boer, J. D. Bourland, J. A. Nyenhuis, C. L. G. Ham, J. M. L. Engels, F. X. Hebrank, G. Frese, and D. J. Schaefer, "Comparison of the threshold for peripheral nerve stimulation during gradient switching in whole body MR systems," *IEEE Trans. Biomed. Eng.*, vol. 15, no. 5, pp. 520–525, 2002.

[6] H. Zhao, S. Crozier, and F. Liu, "Finite difference time domain (FDTD) method for modeling the effect of switched gradients on the human body in MRI," *Magn. Reson. Med.*, vol. 48, pp. 1037–1042, 2002.

[7] A. Hoffmann, S. Faber, K. Werhahn, L. Jager, and M. Reiser, "Electromyography in MRI first recordings of peripheral nerve activation caused by fast magnetic field gradients," *Magn. Reson. Med.*, vol. 43, pp. 534–539, 2000.

[8] B. A. Chronik and M. Ramachandran, "Simple anatomical measurements do not correlate significantly to individual peripheral nerve stimulation thresholds as measured in MRI gradient coils," *Magn. Reson. Med.*, vol. 17, pp. 716–321, 2003.

[9] J. P. Reilly, "Magnetic field excitation of peripheral nerves and the heart: a comparison of thresholds," *Med. and Biol. Eng. and Comput.*, vol. 29, pp. 571–579, 1991.

[10] P. M. Glover and R. Bowtell, "Measurement of electric fields induced in a human subject due to natural movements in static magnetic fields or exposure to alternating magnetic field gradients," *Phys. Med. Biol.*, vol. 53, no. 2, pp. 361–373, 2008.

[11] J. P. Reilly and A. M. Diamant, "Theoretical evaluation of peripheral nerve stimulation during MRI with an implanted spinal fusion stimulator," *Magn. Res. Imag.*, vol. 15, no. 10, pp. 1145–1156, 1997.

[12] D. Buechler, C. Durney, and D. Christensen, "Calculation of electric fields induced near metal implants by magnetic resonance imaging switched gradient magnetic fields," *Magn. Res. Imag.*, vol. 15, no. 10, pp. 1157–1166, 1997.

[13] H. I. Bassen and G. G. Mendoza, "In-vitro mapping of E-fields induced near pacemaker leads by simulated MR gradient fields," *BioMedical Engineering OnLine Vol.* , vol. 8, no. 1, p. 39, 2009.

[14] H. Tandri, M. M. Zviman, S. R. W. T. Lloyd, R. D. Berger, and H. Halperin, "Determinants of gradient field-induced current in a pacemaker lead system in a magnetic resonance imaging environment," *Heart Rhythm Vol.* , vol. 5, no. 3, pp. 462–468, 2008.

[15] E. A. Turk, Y. Z. Ider, and E. Atalar, "Analysis of B_1 mapping by bloch siegert shift," *Proceedings of the 20th Annual Meeting of ISMRM, Melbourne, Australia*, 2012.

[16] E. A. Turk, Y. Z. Ider, A. S. Ergun, and E. Atalar, "Fourier domain approximation for bloch siegert shift," *Proceedings of the 21th Annual Meeting of ISMRM, Salt Lake City, UTAH, USA*, 2013.

[17] L. I. Sacolick, F. Wiesinger, I. Hancu, and M. W. Vogel, "B_1 mapping by bloch-siegert shift," *Magnetic Resonance in Medicine*, vol. 63, no. 5, pp. 1315–1322, 2010.

[18] D. J. Bryant, J. A. Payne, D. N. Firmin, and D. B. Longmore, "Measurement of flow with NMR imaging using a gradient pulse and phase difference technique," *J. Comput. Assist. Tomogr.*, vol. 8, pp. 588–593, 1984.

[19] T. E. Contur and B. H. Robinson, "Analysis of encoding efficiency in MR imaging of velocity magnitude and direction," *Magnetic Resonance in Medicine*, vol. 25, no. 2, pp. 233–247, 1992.

[20] J. F. Debatin, D. A. Leung, S. Wildermuth, R. Botnar, J. Felblinger, and G. C. McKinnon, "Flow quantitation with echo-planar phase-contrast velocity mapping: In vitro and in vivo evaluation," *Journal of Magnetic Resonance Imaging*, vol. 5, no. 6, pp. 656–662, 1995.

[21] P. R. Moran, R. A. Moran, and N. Karstaedt, "Verification and evaluation of internal flow and motion. true magnetic resonance imaging by the phase gradient modulation method.," *Radiology*, vol. 154, no. 2, pp. 433–441, 1985.

[22] M. A. Bernstein, K. F. King, and X. J. Zhou, *Handbook of MRI pulse sequences*. Academic Press, 2004.

[23] R. Muthupillai, P. J. Rossman, D. J. Lomas, J. F. Greenleaf, S. J. Riederer, and R. L. Ehman, "Magnetic resonance imaging of transverse acoustic strain waves," *Magnetic Resonance in Medicine*, vol. 36, no. 2, pp. 266–274, 1996.

[24] O. Lopez, K. K. Amrami, A. Manduca, P. J. Rossman, and R. L. Ehman, "Developments in dynamic MR elastography for in vitro biomechanical assessment of hyaline cartilage under high-frequency cyclical shear," *Journal of Magnetic Resonance Imaging*, vol. 25, no. 2, pp. 310–320, 2007.

[25] E. A. Turk, E. Kopanoglu, Y. Eryaman, V. B. Erturk, and E. Atalar, "Experimental and theoretical analysis of the induced voltage along implant leads due to gradient fields," *Proceedings of the 18th Annual Meeting of ISMRM, Stockholm, Sweden*, 2010.

[26] J. P. Reilly, "Peripheral nerve stimulation by induced electric currents: Exposure to time-varying magnetic fields," *Med. and Biol. Eng. and Comput.*, vol. 27, no. 2, pp. 101–110, 1989.

[27] R. Bowtell and R. Bowley, "Analytic calculations of the E-fields induced by time varying magnetic fields generated by cylindrical gradient coils," *Magn. Reson. Med.*, vol. 44, pp. 782–790, 2000.

[28] F. Liu, L. Xia, and S. Crozier, "Influence of magnetically-induced e-fields on cardiac electric activity during MRI: A modeling study," *Magn. Reson. Med.*, vol. 50, no. 6, pp. 1180–1188, 2003.

[29] F. Rattay, "Analysis of models for the external stimulation of axons," *IEEE Trans. Biomed. Eng.*, vol. 33, no. 10, pp. 974–977, 1986.

[30] J. Jin, *Electromagnetic Analysis and Design in Magnetic Resonance Imaging*. CRC Press LLC, 1999.

[31] R. Turner, "Gradient coil design: A review of methods," *Magn. Res. Imag.*, vol. 11, pp. 903–920, 1993.

[32] M. Abramowitz and I. A. Stegun, *Handbook of Mathematical Functions*. New York: Dover, 1965.

[33] E. Abaci, E. Kopanoglu, V. B. Erturk, and E. Atalar, "Simple analytical equation of the induced E-field," *presented at ISMRM, Toronto, Canada*, 2008.

[34] N. F. Ramsey, "Resonance transitions induced by perturbations at two or more different frequencies," *Physical Review*, vol. 100, no. 4, p. 1191, 1955.

[35] M. M. Khalighi, B. K. Rutt, and A. B. Kerr, "Rf pulse optimization for bloch-siegert B_1+ mapping," *Magnetic Resonance in Medicine*, vol. 68, no. 3, pp. 857–862, 2012.

[36] M. M. Khalighi, B. K. Rutt, and A. B. Kerr, "Adiabatic rf pulse design for bloch-siegert B_1+ mapping," *Magnetic Resonance in Medicine*, 2012.

[37] T. Basse-Lüsebrink, V. Sturm, T. Kampf, G. Stoll, and P. Jakob, "Fast CPMG-based bloch-siegert B_1+ mapping," *Magnetic Resonance in Medicine*, vol. 67, no. 2, pp. 405–418, 2012.

[38] T. C. Basse-Lüsebrink, T. Kampf, A. Fischer, V. J. F. Sturm, D. Neumann, H. Köstler, D. Hahn, G. Stoll, and P. M. Jakob, "Sar-reduced spin-echo-based bloch–siegert B_1+ mapping: BS-SE-BURST," *Magnetic Resonance in Medicine*, vol. 68, no. 2, pp. 529–536, 2012.

[39] M. Saranathan, M. M. Khalighi, G. H. Glover, P. Pandit, and B. K. Rutt, "Efficient bloch-siegert B_1+ mapping using spiral and echo-planar readouts," *Magnetic Resonance in Medicine*, 2013.

[40] M. Jankiewicz, J. C. Gore, and W. A. Grissom, "Improved encoding pulses for bloch-siegert mapping," *Journal of Magnetic Resonance*, 2012.

[41] Q. Duan, P. Gelderen, and J. Duyn, "Improved bloch-siegert based B_1 mapping by reducing off-resonance shift," *NMR in Biomedicine*, 2013.

[42] F. Bloch and A. Siegert, "Magnetic resonance for nonrotating fields," *Physical Review*, vol. 57, no. 6, p. 522, 1940.

[43] G. B. Matson, "An integrated program for amplitude-modulated rf pulse generation and re-mapping with shaped gradients," *Magnetic resonance imaging*, vol. 12, no. 8, pp. 1205–1225, 1994.

[44] E. A. Turk, T. Demir, Y. Z. Ider, A. S. Ergun, and E. Atalar, "Shear wave imaging by using B_1 gradients," *Proceedings of the 21th Annual Meeting of ISMRM, Salt Lake City, UTAH, USA*, 2013.

[45] D. Canet, "Radiofrequency field gradient experiments," *Progress in Nuclear Magnetic Resonance Spectroscopy*, vol. 30, no. 12, pp. 101 – 135, 1997.

[46] G. S. Karczmar, D. B. Tweig, T. J. Lawry, G. B. Matson, and M. W. Weiner, "Detection of motion using B_1 gradients," *Magnetic Resonance in Medicine*, vol. 7, no. 1, pp. 111–116, 1988.

[47] N. Baril, E. Thiaudire, B. Quesson, C. Delalande, P. Canioni, and J.-M. Franconi, "Single-coil surface imaging using a radiofrequency field gradient," *Journal of Magnetic Resonance*, vol. 146, no. 1, pp. 223 – 227, 2000.

[48] G. Karczmar, N. Tavares, and M. Moseley, "Use of radio-frequency field gradients to image blood flow and perfusion in vivo.," *Radiology*, vol. 172, no. 2, pp. 363–366, 1989.

[49] D. Bourgeois and M. Decorps, "A B_1-gradient method for the detection of slow coherent motion," *Journal of magnetic resonance*, vol. 91, no. 1, pp. 128–135, 1991.

[50] R. Kart´ausch, F. Fidler, T. Driele, T. Kampf, T. C. Basse-L´usebrink, U. C. Hoelscher, P. M. Jakob, and X. Helluy, "Spatial phase encoding using a Bloch-Siegert shift gradient," *Proceedings of the 21th Annual Meeting of ISMRM, Salt Lake City, UTAH, USA*, 2013.

[51] J. C. Watkinson, D. Johnston, N. Jones, M. Coady, D. Laws, S. Allen, and J. Hibbert, "The reliability of palpation in the assessment of tumours," *Clinical Otolaryngology and Allied Sciences*, vol. 15, no. 5, pp. 405–409, 1990.

[52] U. Hamhaber, D. Klatt, S. Papazoglou, M. Hollmann, J. Stadler, I. Sack, J. Bernarding, and J. Braun, "In vivo magnetic resonance elastography of human brain at 7 t and 1.5 t," *Journal of Magnetic Resonance Imaging*, vol. 32, no. 3, pp. 577–583, 2010.

[53] I. Sack, J. Rump, T. Elgeti, A. Samani, and J. Braun, "MR elastography of the human heart: Noninvasive assessment of myocardial elasticity changes by shear wave amplitude variations," *Magnetic Resonance in Medicine*, vol. 61, no. 3, pp. 668–677, 2009.

[54] Y. K. Mariappan, K. J. Glaser, and R. L. Ehman, "Magnetic resonance elastography: A review," *Clinical Anatomy*, vol. 23, no. 5, pp. 497–511, 2010.

[55] O. Lopez, K. K. Amrami, A. Manduca, and R. L. Ehman, "Characterization of the dynamic shear properties of hyaline cartilage using high-frequency

dynamic MR elastography," *Magnetic Resonance in Medicine*, vol. 59, no. 2, pp. 356–364, 2008.

[56] A. Arani, D. Plewes, A. Krieger, and R. Chopra, "The feasibility of endorectal MR elastography for prostate cancer localization," *Magnetic Resonance in Medicine*, vol. 66, no. 6, pp. 1649–1657, 2011.

[57] E. I. Ben-Abraham, J. Chen, and R. L. Ehman, "Feasibility of using MR elastography in the intervertebral disc and comparison to finite element model," *Proceedings of the 21th Annual Meeting of ISMRM, Salt Lake City, UTAH, USA*, 2013.

[58] Y. Le, K. Glaser, O. Rouviere, R. Ehman, and J. P. Felmlee, "Feasibility of simultaneous temperature and tissue stiffness detection by MRE," *Magnetic Resonance in Medicine*, vol. 55, no. 3, pp. 700–705, 2006.

[59] T. Oida, A. Amano, and T. Matsuda, "Magnetic resonance elastography: in vivo measurements of elasticity for human tissue," in *Informatics Research for Development of Knowledge Society Infrastructure, 2004. ICKS 2004. International Conference on*, pp. 57–64, 2004.

[60] J. Braun, K. Braun, and I. Sack, "Electromagnetic actuator for generating variably oriented shear waves in MR elastography," *Magnetic Resonance in Medicine*, vol. 50, no. 1, pp. 220–222, 2003.

[61] J. D. Poorter, C. D. Wagter, Y. D. Deene, C. Thomsen, F. Stahlberg, and E. Achten, "Noninvasive MRI thermometry with the proton resonance frequency (PRF) method: In vivo results in human muscle," *Magnetic Resonance in Medicine*, vol. 33, no. 1, pp. 74–81, 1995.

[62] D. Plewes, C. Luginbuhl, C. Macgowan, and I. Sack, "An inductive method to measure mechanical excitation spectra for MRI elastography," *Concepts in Magnetic Resonance Part B: Magnetic Resonance Engineering*, vol. 21B, no. 1, pp. 32–39, 2004.